The Interaction of Jets with Crossflow

Krishnan Mahesh

Department of Aerospace Engineering and Mechanics, University of Minnesota, Minneapolis, Minnesota 55455; email: mahesh@aem.umn.edu

Annu. Rev. Fluid Mech. 2013. 45:379–407

First published online as a Review in Advance on October 5, 2012

The *Annual Review of Fluid Mechanics* is online at fluid.annualreviews.org

This article's doi: 10.1146/annurev-fluid-120710-101115

Keywords

incompressible, supersonic, structure, entrainment, mixing

Abstract

It is common for jets of fluid to interact with crossflow. This article reviews our understanding of the physical behavior of this important class of flow in the incompressible and compressible regimes. Experiments have significantly increased in sophistication over the past few decades, and recent experiments provide data on turbulence quantities and scalar mixing. Quantitative data at high speeds are less common, and visualization still forms an important component in estimating penetration and mixing. Simulations have progressed from the Reynolds-averaged methodology to large-eddy and hybrid methodologies. There is a general consensus on the qualitative structure of the flow at low speeds; however, the flow structure at low-velocity ratios (jet speed/crossflow speed) might be fundamentally different from the common notion of shear-layer vortices, counter-rotating vortex pairs, wakes, and horseshoe vortices. Fluid in the near field is strongly accelerated, which affects the jet trajectory, entrainment, and mixing behavior. At low speeds, mixing depends more on Reynolds number than the jet trajectory or spatial extent does. Turbulence kinetic energy budgets are discussed that reveal the considerable nonequilibrium nature of the flow and the consequent challenges posed to time-averaged prediction methodologies. The parameter space at high speeds is fairly large, and even experimentally derived correlations for trajectories show significant scatter. Coherent motions in high-speed jets are seen to entrain large amounts of crossflow fluid but do not mix effectively in the near field.

1. INTRODUCTION

The term jet in crossflow refers to a jet of fluid that exits an orifice to interact with the surrounding fluid that is flowing across the orifice. **Figure 1*a*** shows a schematic of the canonical jet in crossflow, in which a circular jet is interacting with a crossflow on a flat plate. Also known as transverse jets, jets in crossflow are common in both nature and human-made devices. In gas-turbine combustors, jets of cool air exit dilution holes in the combustor (see **Figure 1*b***), where they mix with the hot combustion products and yield more uniform exit temperatures. In the primary combustion zone, the dilution jets are used to change the ratio of air to fuel and thereby reduce nitrogen-oxide levels in the exhaust. The efficiency of gas-turbine engines increases with increasing temperatures at the inlet to the high-pressure turbine stage. As a result, inlet temperatures in modern engines can exceed the melting point of the turbine blade material. Turbine blades are therefore film cooled; that is, arrays of low-velocity air jets exit holes in the turbine blades to cool the blades and protect them from the high-temperature crossflow. In contrast to dilution jets, for which it is desirable to have the jets aggressively spread and penetrate the crossflow, film-cooling jets are required to penetrate less and adhere to the surface of the blades as much as possible.

Figure 2*a* shows an image of the X-43A research vehicle, which in 2004 became the first scramjet-engine-powered aircraft to successfully operate in flight (McClinton 2006). The entry Mach number to a scramjet combustor is nominally one-third of the flight Mach number; the flow inside the combustor is therefore supersonic (less than Mach 5) for flight Mach numbers less than 15. The successful operation of high-speed propulsion systems depends critically on the efficient mixing and combustion of fuel and air during the very short residence times inside the combustor. Transverse injection of the fuel jet into crossflowing air has shown promise in this regard. Another high-speed application of transverse jets is their use in thrust vector control. **Figure 2*b*** shows the launch abort system for the Orion space vehicle (NASA). The system has an abort motor with four downfiring jets, an attitude-control motor with eight circumferentially arranged side-firing jets, and a jettison motor. During an abort, the jets fire simultaneously to control the accelerating vehicle. Interaction of the jet plumes with the subsonic/supersonic crossflow, each other, and the body of the vehicle impacts vehicle controllability.

Volcanic eruptions can result in jet plumes (**Figure 3*a***) that are transported by the crosswind to form deposits miles away from their source. The Fisher Tuff in Alaska is one such example, which has been widely studied for its unique deposits on the leeward side of a large mountain range, 10–15 km away from the Fisher volcano (Gardner et al. 2007). Crosswind also affects the height to which the volcanic plume rises, which can be several miles, and how ash, smoke, and other volcanic matter are dispersed in both the atmosphere and surrounding areas. Crossflow similarly

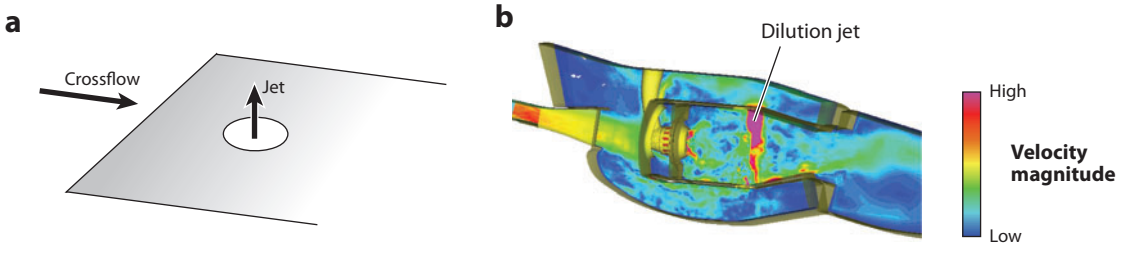

Figure 1

(*a*) A schematic of a circular jet issuing into crossflow over a flat plate. (*b*) Instantaneous snapshot of contours of velocity magnitudes from large-eddy simulations in a gas-turbine combustor (Mahesh et al. 2004). Note the strong dilution jets at the top and bottom.

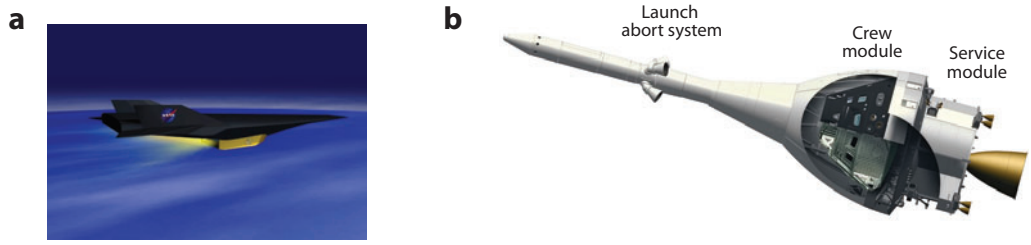

Figure 2

(*a*) Image of the X-43A research vehicle after separation from the Pegasus booster. Panel *a* taken from the NASA Dryden Flight Research Photo Collection. (*b*) Rendering of the Orion Launch Abort System during an abort test. Panel *b* courtesy of NASA.

influences the trajectory and dispersal of plumes arising from fires (**Figure 3*b***), effluent discharge, and smokestacks.

A fascinating example of transverse jets in nature involves bivalve clams and blue crabs. Water passes through the clams, picks up waste metabolites, and issues out in a jet-like flow. The jet interacts with the cross-stream to form a plume containing the metabolites, which are sensed by predators such as blue crabs, which then track the clams (Delavan & Webster 2011). Central venous catheters are used in hemodialysis to remove contaminated blood and replace it with processed blood. The catheters are typically placed in the superior vena cava, and the jet that exits a hole at the catheter tip interacts with the crossflow in the vena cava and the vena cava walls in a fairly unsteady and complex manner. This interaction has been linked to health-risk complications that occur during catheter use (Foust & Rockwell 2006).

This article reviews our fundamental understanding of transverse jets in both incompressible and compressible regimes. It is restricted to single-phase, nonreacting jets injected flush into the crossflow. Sections 2 and 3 discuss incompressible and compressible transverse jets, respectively.

2. INCOMPRESSIBLE JETS IN CROSSFLOW

2.1. Overview

Using ρ_j and ρ_∞ to denote the densities of jet and crossflow fluids, and U_j and U_∞ to denote their mean velocities, one can describe the following nondimensional parameters for incompressible

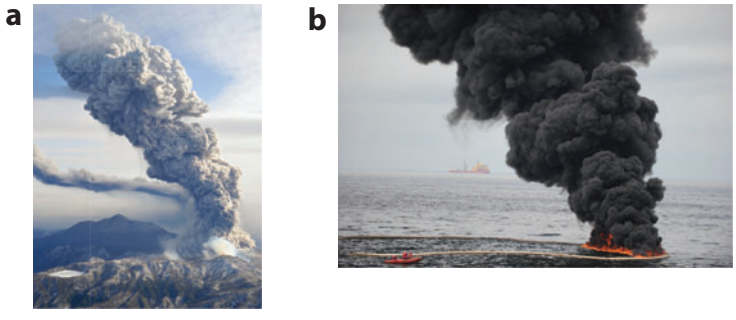

Figure 3

(*a*) Plume from the Kirishima volcano in Japan on January 26, 2011. Photograph courtesy of the Associated Press. (*b*) Oil fire plume. Photograph by Justin E. Stumberg, US Navy.

transverse jets,

$$r = U_j/U_\infty, \quad J = \rho_j U_j^2/\rho_\infty U_\infty^2, \quad \text{and} \quad Re_j = U_j d/\nu_j, \tag{1}$$

where r is the velocity ratio, J denotes the momentum flux ratio, and Re_j is the jet Reynolds number. Additional parameters include the ratio of the crossflow boundary-layer thickness to the jet diameter δ/d, and the velocity profiles of the jet and crossflow boundary layer. Early studies were motivated by smokestack plumes and atmospheric dispersion (e.g., Sutton 1932, Bosanquet & Pearson 1936). Sutton (1932) discussed a model to predict/explain the observed wind distribution over Northern Europe. By deriving a formula for "concentration at ground level due to a line source of smoke/pollutant/mass at finite height," Bosanquet & Pearson (1936) attempted to estimate the contaminants on the ground resulting from power-station chimneys. They concluded that for regions far away from the contamination source, the height of the chimney has no recognizable impact.

The sophistication and detail of the experiments resolving this flow field have dramatically increased. Similarly, flow simulations have progressed from Reynolds-averaged computations to direct numerical simulations (DNS) and large-eddy simulations (LES). The earliest experimental studies measured jet trajectories for different flow conditions (e.g., Pratte & Baines 1967). Subsequent studies collected mean flow and turbulence data using hot wires and laser Doppler anemometry, with Ramsey & Goldstein (1970) and Crabb et al. (1981) among the first. Triple-wire probes were used by Andreopoulos & Rodi (1984) to simultaneously measure all three velocity components. Other experimental techniques include hot films (Sherif & Pletcher 1989), smoke illuminated by lasers (Fric & Roshko 1994), hydrogen bubbles (Kelso & Smits 1995), flying hot wires (Kelso et al. 1996), and most recently particle image velocimetry and planar laser-induced fluorescence (Haven & Kurosaka 1997, Smith & Mungal 1998, Su & Mungal 2004, Shan & Dimotakis 2006). The canonical transverse jet is round, but noncircular jets have been considered by some studies (e.g., Liscinsky et al. 1995, Haven & Kurosaka 1997, New et al. 2003, Gutmark et al. 2008).

Early work on this problem examined what might be considered first-order issues (i.e., scaling laws for the mean jet trajectory, and the decay of a passive scalar in the jet). Based on collected data, Pratte & Baines (1967) proposed a length scale rd to collapse the jet trajectory. Keffer & Baines (1963) proposed $r^2 d$ as a length scale to collapse jet trajectories for velocity ratios of six to ten up to eight diameters from the jet exit. These correlations are still used to scale jet trajectories (Margason 1993). Fewer studies have examined scalar mixing. Patrick (1967) appears to have been among the earliest, with Smith & Mungal (1998), Su & Mungal (2004), and Shan & Dimotakis (2006) more recent. Most other work on this problem has focused on the origin and behavior of coherent structures in this flow (e.g., Moussa et al. 1977, Andreopoulos & Rodi 1984, Karagozian 1986, Sykes et al. 1986, Coelho & Hunt 1989, Krothapalli et al. 1990, Kelso et al. 1996). Recent computational studies have used LES or DNS to predict the canonical jet in crossflow (e.g., Yuan et al. 1999; Muppidi & Mahesh 2005, 2007, 2008; Iourokina & Lele 2006; Sau & Mahesh 2010). Recent computational and experimental studies have demonstrated the utility of having three-dimensional unsteady data to examine the physics of the flow.

2.2. Qualitative Time-Averaged Behavior

An indication of the time-averaged behavior of transverse jets is provided in **Figure 4**, which shows results from DNS (Muppidi & Mahesh 2007) of an $Re_j = 5{,}000$, $r = 5.7$ jet. The simulations were performed under the same conditions as experiments by Su & Mungal (2004), with which they showed good agreement. The contours of the mean velocity demonstrate that the jet bends

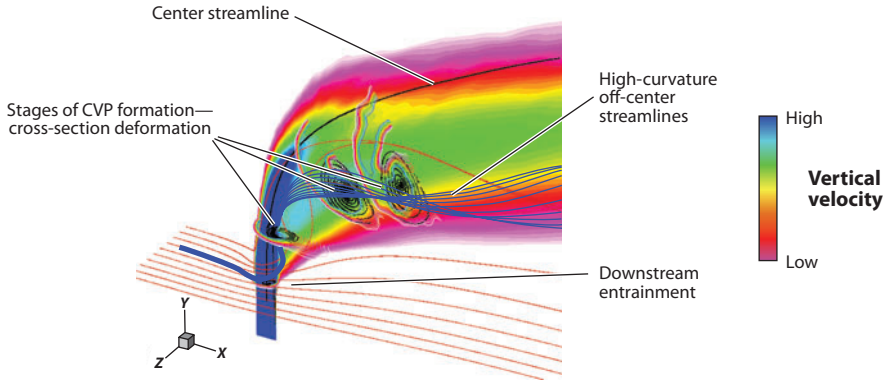

Figure 4

The mean flow for an incompressible transverse jet. Contours of the vertical velocity are shown on the symmetry plane along with the center streamline. Jet cross sections at $s = d$, $4d$, $10d$, and $15d$ are shown using contours of u_s and streamlines of the in-plane velocity. Figure taken from Muppidi & Mahesh (2007). Abbreviation: CVP, counter-rotating vortex pair.

in the direction of the crossflow and increases in width as it moves downstream. We note that the jet is wider toward the leeward side than toward the windward side of the center streamline. Moreover, the cross section of the jet evolves from its circular shape to form a counter-rotating vortex pair (CVP). The local mean vorticity is maximum at the CVP center, which lies below the center streamline. The jet trajectory based on the center streamline therefore penetrates deeper into the crossflow than a trajectory based on the vorticity, as noted by Fearn & Weston (1974). Similar behavior is displayed by jet trajectories based on maxima of the scalar concentration in the jet cross section (Kamotani & Greber 1972, Yuan et al. 1999, Su & Mungal 2004), as more of the scalar would be entrained and mixed toward the center of the CVP.

2.3. Qualitative Instantaneous Behavior

The instantaneous behavior of a jet is unsteady and violent. As the jet fluid approaches the exit, it experiences an adverse pressure gradient on the windward side of the pipe owing to the high-pressure region created above the jet exit by the crossflow. As a result, the jet fluid at the leading edge of the pipe decelerates at high-velocity ratios and separates inside the pipe at low-velocity ratios (Kelso et al. 1996, Muppidi & Mahesh 2005). Mass conservation therefore causes the exit velocity profiles of the jet to be skewed toward the leeward side. The crossflow boundary layer separates ahead of the jet and moves around the jet while attempting to accelerate the jet in the streamwise direction. The jet shear layer is therefore skewed and is not a constant pressure-gradient shear layer. Jet shear-layer vortices are typically observed on the windward side of the jet (**Figure 5*a***). They bear resemblance to Kelvin-Helmholtz rollers in regular jets, are highly unsteady, and are not observed in the time-averaged solution. In general, both small-scale turbulence and large-scale coherent features are observed. Several coherent vortex systems have been identified and are discussed below.

2.3.1. Counter-rotating vortex pairs. The CVP has long been considered a signature feature of jets in crossflow and persists far downstream. Indeed, thrust vectoring of projectiles using transverse jets can be adversely affected by the CVP interacting with solid surfaces on the projectile.

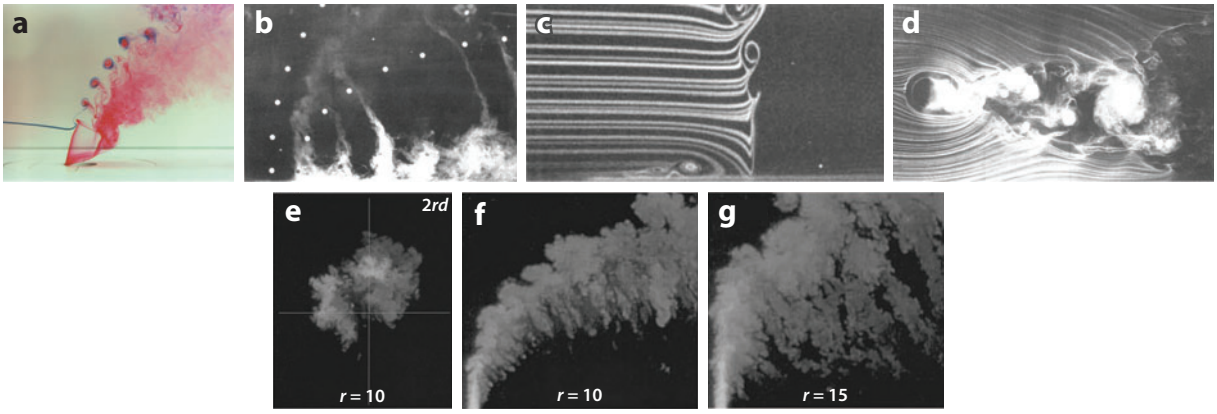

Figure 5

Visualizations of instantaneous flow structures. (*a*) Shear-layer vortices. Panel *a* taken from Kelso et al. (1996). (*b*) Tornado-like wake vortices. (*c*) Cross section of hairpin vortices upstream of the jet in the symmetry plane. (*d*) Wall-parallel cross section, illustrating hairpin and wake vortices. Panels *b–d* taken from Fric & Roshko (1994). (*e*) Instantaneous counter-rotating vortex pair visualization of jet fluid in a wake at (*f*) $r = 10$ and (*g*) $r = 15$. Panels *e–g* taken from Smith & Mungal (1998).

The CVP is highly unsteady and asymmetric instantaneously (**Figure 5*e***). Early experiments that examined the jet cross section were those by Kamotani & Greber (1972), who observed how, far downstream, the original jet seemed to disappear while a pair of vortices dominated the flow field. CVP formation is delayed as the jet velocity ratio increases. Smith & Mungal's (1998) experiments found that CVP formation is slower (based on the distance from the jet exit normalized with rd) at $r = 20$ compared with $r = 10$.

Different mechanisms leading to the CVP have been suggested. Broadwell & Breidenthal (1984) viewed the jet as imparting an impulse to the crossflow, which yields a CVP similar to how tip vortices are produced behind finite lifting wings (**Figure 6*a***). Although attractive in its elegance, and practical in its ability to yield a scaling law for the jet trajectory, this explanation is fundamentally different from the general consensus that CVP formation results from modification of the jet vorticity by the crossflow and is initiated in the near field (e.g., Moussa et al. 1977, Andreopoulos & Rodi 1984, Sykes, Lewellen & Parker 1986, Coelho & Hunt 1989). Based on observations from experiments at velocity ratios between 2.0 and 6.0, and Reynolds numbers between 440 and 6,200, Kelso et al. (1996) suggested schematically (**Figure 6*b***) how "tilting and folding" of the jet shear layer contribute to the circulation of the CVP. Their proposal is in general agreement with the vortex-element simulations of Cortelezzi & Karagozian (2001) in a domain that does not include a pipe. Vortex-element simulations were also used by Marzouk & Ghoniem (2007) to suggest that initially planar vortex rings generated close to the jet exit stretch upward on the leeward side, which aligns the vorticity in the direction of the crossflow, yielding the CVP. A pressure-based explanation was proposed by Muppidi & Mahesh (2006) using a two-dimensional model problem (**Figure 6*c***) in which a circular region of out-of-plane flow interacts with an in-plane crossflow. The circular region evolves into a CVP, which they explain in terms of the initial acceleration that the jet fluid experiences in the direction of the crossflow. They suggest that the near field of a transverse jet is pressure driven while the far field is momentum driven. That the simulations described above yield a CVP in the absence of a pipe suggests that as far as CVP formation is concerned, the pipe might be important only to the extent that it provides the flux of vorticity that is modified by the crossflow to yield a CVP.

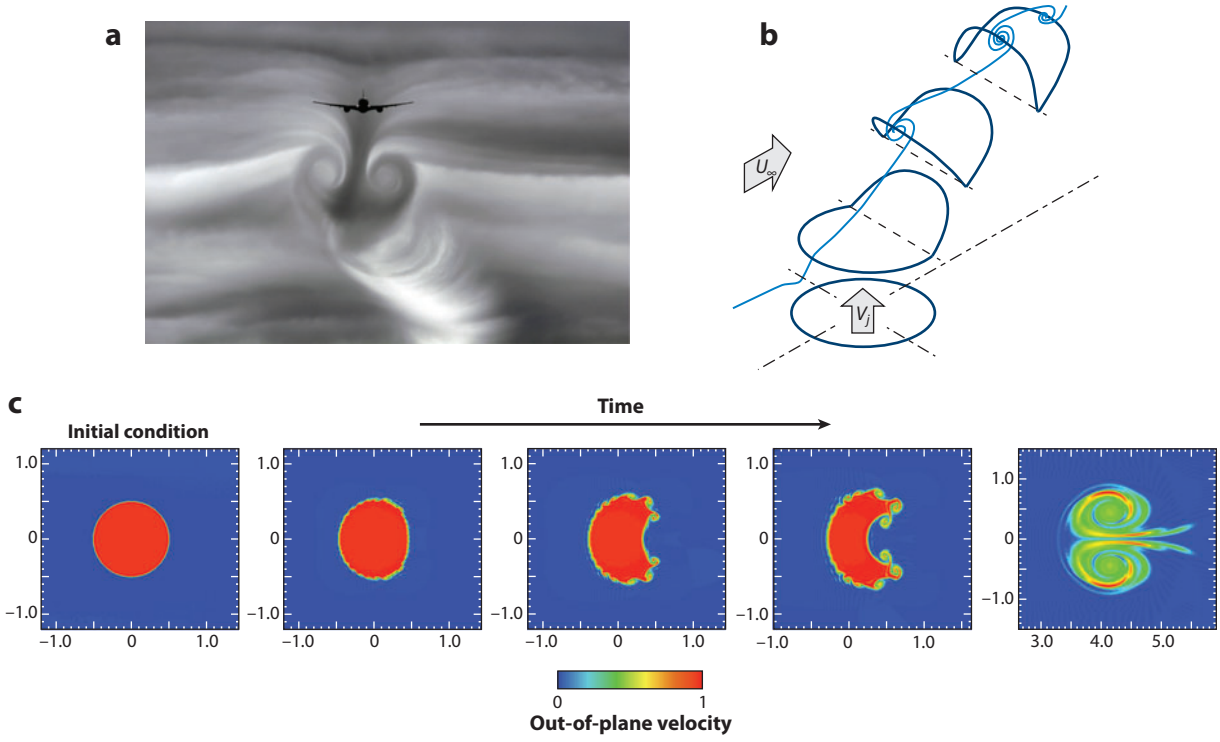

Figure 6

(*a*) Visualization of trailing vortices induced by aircraft. Panel *a* courtesy of AirTeamImages Limited (**http://www.airteamimages.com**). (*b*) Schematic of how a near-field vortex ring is distorted to produce a counter-rotating vortex pair (CVP). Panel *b* taken from Kelso et al. (1996). (*c*) Evolution of circular region of out-of-plane velocity (*color contours*) into a CVP upon acceleration by crossflow. Panel *c* taken from Muppidi & Mahesh (2006).

2.3.2. Horseshoe and wake vortices. Horseshoe vortices form upstream of the jet's leading edge and persist downstream (**Figure 5*c*,*d***). These vortices form because the crossflow boundary layer encounters an adverse pressure gradient upstream of the jet, separates, and forms spanwise vortices (**Figure 5*c***) that move around the jet. Krothapalli et al. (1990) studied horseshoe vortices upstream of a rectangular jet in crossflow and noted that the formation and rollup of the vortices can be periodic. Kelso & Smits (1995) showed that the vortex system can be steady, oscillate, or coalesce depending on the velocity ratio, r. Both studies note the similarity between the unsteadiness of the horseshoe vortex system and unsteadiness in the wake.

Wake vortices are the upright vortices observed downstream of the jet, extending from the wall to the leeward side of the jet (**Figure 5*b*,*d***). When visualized in planes parallel to the wall, the vortices resemble the vortex street observed behind solid cylinders (**Figure 5*d***). However, as noted by Fric & Roshko (1994), the wake of a transverse jet is noticeably different from that of a circular cylinder at the same Reynolds number. By introducing smoke in the crossflow boundary layer, and from spectral measurements, they suggested that the wake vortices originate from separation events in the crossflow boundary layer downstream of the jet. Vortex-element simulations by Schlegel et al. (2011) showed similar behavior. However, filaments of jet fluid have been observed in the jet wake (**Figure 5*f*,*g***) by Smith & Mungal (1998) (r varies from 5 to 20), by Su & Mungal (2004) ($r = 5.7$) and by Shan & Dimotakis (2006) ($r = 10, 32$). Vorticity from the jet shear layer

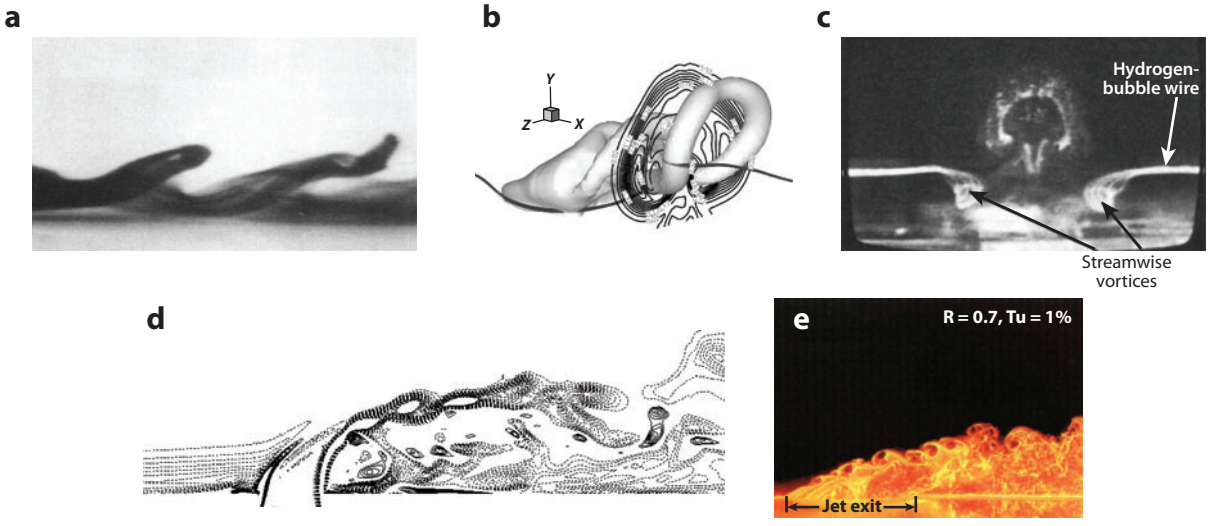

Figure 7

Visualization of hairpin vortices. (*a*) An $r = 0.1$ jet from a narrow rectangular slot. (*b*) An $r = 1$ round jet. (*c*) End view of the flow. (*d*) Vorticity contours in the symmetry plane. (*e*) Two-color PIV images in the symmetry plane. Panels *a* and *c* taken from Acarlar & Smith (1987), panels *b* and *d* taken from Sau & Mahesh (2008), and panel *e* taken from Gogineni et al. (1996).

has also been observed in the jet wake at low-velocity ratios ($r < 2$) (Gopalan et al. 2004). The different vortex systems can interact. For example, Kelso et al. (1996) suggested that horseshoe vortices with the same sign of vorticity as that of the crossflow boundary layer extend along the wall and are incorporated into the wake vortex system. Those with the opposite sign lift away from the wall and are absorbed into the CVP.

2.3.3. A different flow structure at low-velocity ratios. As discussed above, transverse jets generally comprise shear-layer vortices on the windward side, CVPs, horseshoe vortices, and wake vortices. However, their structure at low-velocity ratios (nominally less than 1) is different. In this regime, the interaction of the jet with the crossflow is dominated by hairpin vortices. **Figure 7*a*** shows a side view of the flow downstream of injection, observed by Acarlar & Smith (1987) upon injecting fluid into a laminar boundary layer from a narrow, streamwise-oriented rectangular slot. We note the train of hairpin vortices produced. In fact, the goal of the experiment was to produce hairpin vortices from low-momentum streaks near the wall. Acarlar & Smith's velocity ratios were of the order of 0.1. **Figure 7*b*** shows results from simulations by Sau & Mahesh (2008) for a round jet with $r = 1$, demonstrating similar hairpins. The hairpins form because vorticity at the leading edge of the pipe exit has opposite sign to the vorticity of the crossflow boundary layer. At low-velocity ratios, the boundary-layer vorticity can overwhelm the leading-edge vorticity in the pipe, resulting in vorticity essentially being shed from the trailing edge. At low Reynolds numbers, the hairpin vortices are coherent and periodic; at higher Reynolds numbers, they become unstable as they evolve but are still visible. The hairpins are not apparent if the flow is visualized in the symmetry plane and streamwise planes alone. As seen in **Figure 7*b*,*c***, the streamwise plane shows what looks like a CVP but is in fact the flow produced by the hairpin legs. Similarly, the symmetry plane shows what look like shear-layer vortices but are in fact a cross section of the hairpin heads (**Figure 7*d*,*e***).

2.4. Jet Trajectory

The mean jet trajectory describes the extent to which the jet penetrates into the crossflow. The jet trajectory can be defined in different ways: as positions of local velocity maxima, local scalar maxima, vorticity maxima, or as the time-averaged streamline originating at the jet exit. As discussed in Section 2.2, different definitions can yield slightly different trajectories, especially in the far field. Smith & Mungal (1998) found that their trajectories based on the maximum local velocity penetrate 5–10% deeper into the flow than trajectories based on the maximum scalar concentration. Jet trajectories are most commonly scaled with rd; i.e.,

$$\frac{y}{rd} = A\left(\frac{x}{rd}\right)^B, \tag{2}$$

where A and B are constants. Margason (1993) provided a list of experimental values for A and B, which shows $1.2 < A < 2.6$ and $0.28 < B < 0.34$. rd may be considered a global length scale (Broadwell & Breidenthal 1984) when a transverse jet is treated as a point source of momentum flux and viewed from the far field. Broadwell & Breidenthal (1984) modeled the far field of the jet as a streamwise vortex pair that moves at free-stream velocity. The jet is treated as a point source of normal momentum; i.e., the jet mass flow rate m_j and jet diameter d_j approach zero while U_j increases such that the jet momentum flux $m_j U_j$ remains constant. Dimensional arguments then yield the length scale

$$l = \left(\frac{m_j U_j}{\rho_\infty U_\infty^2}\right)^{1/2}. \tag{3}$$

If the density of the jet and that of crossflow are equal, l is equal to $(\pi/4)^{(1/2)}\, rd$. The vortices induce a velocity on each other, $dy/dt \propto \Gamma/R$, where $2R$ is the separation distance. Their circulation Γ is related to the impulse per unit length, $P = m_j U_j / U_\infty \propto \rho_\infty \Gamma r$. The requirement of self-similarity in the far field necessitates that $r \propto y$, which allows dy/dt to be integrated to obtain the following insightful expressions:

$$\frac{y}{l} \propto \left(\frac{x}{l}\right)^{1/3}, \quad \frac{\Gamma}{U_\infty l} \propto \left(\frac{x}{l}\right)^{-1/3}. \tag{4}$$

The assumptions made in Broadwell & Breidenthal's analysis are reasonable in the far field, in which the CVP is fully formed, and the jet does not experience any acceleration. In the near field of the jet exit, the jet initially has negligible horizontal velocity; the crossflow therefore accelerates the jet fluid in the horizontal direction, deforming its cross section in the process. What constitutes the far field is unclear, although Smith & Mungal (1998) suggested a far-field definition of $x/r^2 d > 0.3$. A velocity ratio of 10 therefore corresponds to the establishment of the far field at 30 diameters. For internal flows such as dilution jets or fuel-injection ports, the near-field behavior is probably more relevant.

Other scalings have been proposed. Keffer & Baines (1963) observed trajectories from their experiments to collapse with $r^2 d$. Their data were in a region close to the jet exit (a maximum downstream distance of $4d$). Karagozian (1986) considered a vortex pair issuing from the jet orifice into the crossflow. Numerical solution of the equations governing the evolution of this vortex pair yields

$$\frac{y}{d} = \alpha r^\beta \left(\frac{x}{d}\right)^\gamma \tag{5}$$

for the trajectory, where $\alpha = 0.527$, $\beta = 1.178$, and $\gamma = 0.314$. Smith & Mungal (1998) performed experiments at velocity ratios ranging from 5 to 25 and suggested that rd is preferable over d or $r^2 d$ to scale the trajectories. They suggested $r^2 d$ as a length scale that distinguishes near-field and far-field behavior. Hasselbrink & Mungal (2001) used similarity theory to

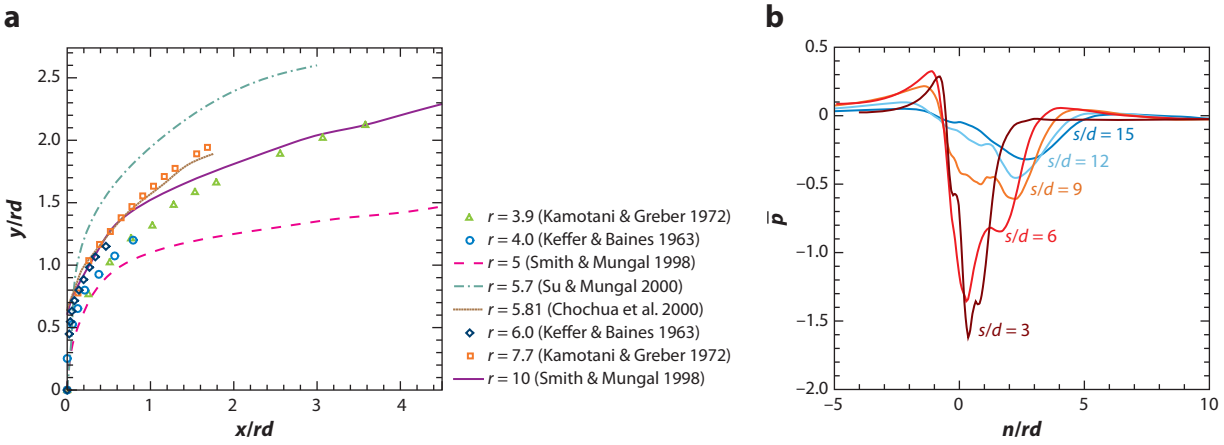

Figure 8

(*a*) Jet trajectories from different experiments scaled by *rd*. Panel *a* from Muppidi & Mahesh (2005). (*b*) Profiles of mean pressure from DNS of Muppidi & Mahesh (2007), illustrating the pressure gradient across the jet in the near field. *n* is the coordinate normal to the jet trajectory.

suggest

$$\frac{y}{rd} = \left\{ \frac{2}{c_{ej}} \frac{x}{rd} \right\}^{1/2} \quad \text{and} \quad \frac{y}{rd} = \left\{ \frac{3}{c_{ew}} \frac{x}{rd} \right\}^{1/3} \tag{6}$$

in the near field and the far field, respectively. Here c_{ej} and c_{ew} are the entrainment coefficients in the jet region and the wake-like region, respectively.

There is evidence that *rd* is not sufficient to scale a wide range of data. Smith & Mungal's (1998) scaled trajectories show noticeable variation for jets, with *r* varying from 5 to 20. In fact, the scatter appears comparable to trajectories scaled with $r^2 d$. There can be considerable differences in scaled trajectories from experiments with fairly similar velocity ratios (e.g., 5.7 and 5.81) (see **Figure 8*a***). A laminar jet penetrates more than a turbulent jet does with the same velocity ratio. Similarly, a thicker crossflow boundary layer allows the jet to penetrate more (Muppidi & Mahesh 2005). The trajectories of Su & Mungal's (2004) ($r = 5.7$) experiment with a pipe-generated jet differ from those of Smith & Mungal's (1998) ($r = 5$) nozzle-generated jet at fairly similar velocity ratios. Muppidi & Mahesh (2005) suggested that jet trajectory depends not just on the velocity or momentum ratio, but also on the distribution of momentum in both the jet and crossflow boundary layer. They suggest the scaling

$$\frac{y}{rd} = A' \left(\frac{x}{rd} \right)^B \left(\frac{h}{d} \right)^C, \tag{7}$$

where *h* is a near-field length scale, which is given by

$$\frac{h}{d} = \left\{ \frac{3}{4} \pi C_m r^2 \frac{\delta^2 d_j^2}{d^4} \right\}^{\frac{1}{3}} \quad \text{when} \quad h \le \delta, \quad \text{and}$$

$$\frac{h}{d} = \frac{2}{3} \frac{\delta}{d} + \frac{\pi}{4} C_m r^2 \frac{d_j^2}{d^2} \quad \text{when} \quad h \ge \delta. \tag{8}$$

Here C_m is constant and $\int u_j^2 dA = \frac{\pi d_j^2}{4} U_j^2$.

2.5. Entrainment

A transverse jet is better than a regular free jet at entraining and mixing with the surrounding fluid. Compared to a free jet, the decay in the centerline velocity and jet fluid concentration of a transverse jet is generally more rapid (Moussa et al. 1977, Smith & Mungal 1998) in the near field and slower in the far field. Smith & Mungal's (1998) experiments, which seeded an air jet with acetone and used planar laser-induced fluorescence imaging to measure the concentration, show that over a range of velocity ratios from 5 to 25, the peak jet fluid concentration in the center plane initially remains constant and then decays at a rate proportional to $s^{-1.3}$ in the near field. In contrast, a free jet would decay at a rate s^{-1}.

Broadwell & Breidenthal's (1984) analysis suggests that the decay in the centerline concentration in the far field of a transverse jet should be proportional to $x^{-2/3}$, which is less than that for a free jet. We note that far downstream, a transverse jet would have more of a wake-like profile. Smith & Mungal's (1998) data show the far-field decay rate to be distinctly lower than $s^{-1.3}$; however, the slopes are not necessarily $-2/3$ for all velocity ratios. Lower-velocity-ratio jets appear to exhibit this reduced decay rate earlier than the higher-velocity-ratio jets. This behavior appears to not be universal. For example, Su & Mungal's $r = 5.7$ jet from a circular pipe exhibits a decay rate higher than -1 at $rd = 0.5$–0.9, near a -1 decay rate until $rd = 2.5$, and a significantly higher decay rate beyond 2.5 until the end of the measurements.

One conclusion drawn from this behavior is that scalar mixing is sensitive to the jet-exit conditions and near-field behavior. However, such behavior could also result from the three-dimensionality of the flow and the impropriety of only using trajectories in the symmetry plane. A free jet is axisymmetric, and both the velocity and concentration are maximum at the axis of symmetry. In contrast, for a transverse jet, as the CVP fully forms, the maximum concentration levels move out of the symmetry plane; even in the symmetry plane, the peak concentration and velocity locations do not coincide. It is probably more appropriate therefore to use global measures such as the entrainment rate.

The entrainment of a turbulent axisymmetric free jet is described by the Ricou-Spalding correlation (Ricou & Spalding 1961, Han & Mungal 2001, Babu & Mahesh 2004),

$$\frac{\dot{m}}{\dot{m}_0} = 1 + 0.32\frac{s}{d}. \tag{9}$$

For transverse jets, assuming far-field trajectories and considering the momentum transfer needed to attain the trajectory, Hasselbrink & Mungal (2001) proposed

$$\frac{\dot{m}}{\dot{m}_0} = 1 + \frac{r}{AB}\left(\frac{x}{rd}\right)^{1-B}. \tag{10}$$

Specifying r and comparing Equations 9 and 10 as functions of x, one can see that the transverse jet has higher mass flow rates for the same initial m_0. Knowing the far-field entrainment rate allows the mean scalar concentration in the far field to be estimated (e.g., Shan & Dimotakis 2006) assuming $u \sim U_\infty$, $\dot{m}/\dot{m}_0 \approx 1/\overline{C}$. Muppidi & Mahesh (2008) computed entrainment from their DNS of Su & Mungal's (1998) experiments. The jet fluid is marked by a passive scalar, and the entrainment of the crossflow fluid by the jet is estimated from the volume flux of the scalar-carrying fluid across the trajectory-normal planes. **Figure 9*a*** shows the variation of the volume flux with distance from the jet exit along with the Ricou-Spalding correlation for a free jet. Entrainment in the transverse jet is significantly larger than that in a regular jet. The transverse jet displays higher entrainment rates past $2d$ (i.e., in the near field itself), and at $6d$, the mass flow rate in the transverse jet is already approximately twice that in a regular jet.

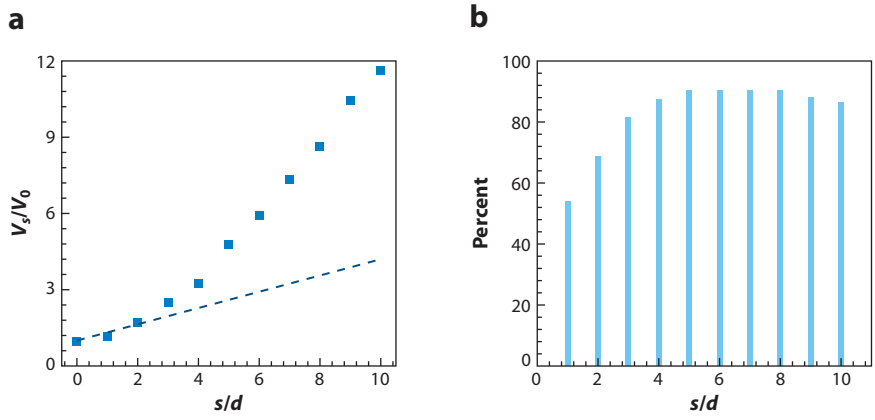

Figure 9

The entrainment rate of a transverse jet. (*a*) Variation of the volume flux of a scalar-carrying fluid along the length of the jet. The symbols represent data from Muppidi & Mahesh (2008), and the dashed line is the Ricou-Spalding (1961) correlation for a free jet. (*b*) Percentage contribution of the downstream side of the jet to the total entrainment. Figure taken from Muppidi & Mahesh (2007).

Figure 9*b* shows the percentage contribution of the downstream side of the jet to the total entrainment. Close to the jet exit, both the downstream and upstream sides of the jet contribute about the same amount to the total entrainment, and in this region, the transverse jet's entrainment is roughly the same as that of a regular jet (**Figure 9*a***). Further downstream, the contribution of the downstream side increases significantly. It appears that the increased entrainment of the transverse jet as compared with that of the regular jet past $2d$ corresponds to the increased contribution of the downstream side of the jet to the total entrainment. This behavior is explained by Muppidi & Mahesh (2008) as being caused by the crossflow going around the jet and impinging on the symmetry plane to produce the saddle node observed by Kelso et al. (1996). The resulting high pressure at the saddle node drives downstream fluid into the jet. More data are needed to assess how these observations for $r = 5.7$ apply to other velocity ratios and jet-exit conditions.

2.6. Mixing

Entrainment of the crossflow fluid produces sharp fronts in the concentration. Turbulent advection then increases the surface area of the fronts to a point at which viscosity consumes them. As noted above, mean concentration levels describe entrainment. Mixing is described by measures such as the probability density function (PDF) of the concentration. Moreover, mixed-fluid concentrations appear more sensitive to Reynolds number than trajectories, the decay of the mean concentration on the centerline, and the spatial extent of the jet.

Mixing in the near field of transverse jets (at least for $r \geq 10$) is quantitatively different from that in the far field, as shown by the PDFs measured by Smith & Mungal (1998) for transverse air jets. Their data for $r \geq 10$ show that in the near field (**Figure 10*a***), the PDFs of mixture fractions display a preferred concentration that does not significantly vary along the radial width of the jet (between lines L_1 and L_2 in the figure), whereas the far-field PDFs (**Figure 10*b***) exhibit a preferred concentration that decreases (moves toward the free-stream concentration) as the PDF is measured further from the jet center.

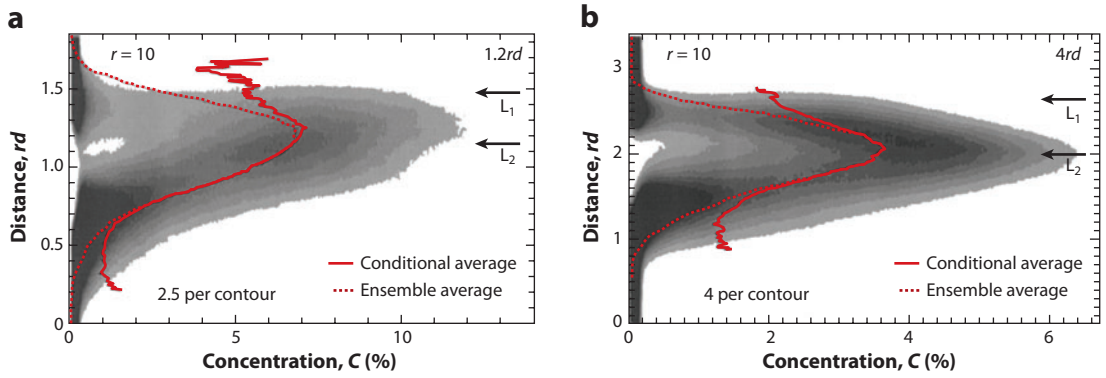

Figure 10

Probability density function of mixture fractions for an $r = 10$ transverse jet in the (*a*) near field and (*b*) far field. Figure taken from Smith & Mungal (1998).

The Reynolds number dependence of scalar fluctuations in regular turbulent jets has been summarized by Dimotakis (2000), who showed $c_{\mathrm{rms}}/\bar{c}$ at the jet centerline as a function of jet Reynolds number for liquid-phase and gas-phase jets. The data show that $c_{\mathrm{rms}}/\bar{c}$ at the jet centerline decreases with increasing Reynolds number and reaches an asymptotic value at sufficiently high Reynolds number. Gas-phase jets are observed to be less sensitive to Reynolds number than liquid-phase jets over the range of Reynolds numbers shown.

Shan & Dimotakis (2006) performed concentration measurements using laser-induced fluorescence in transverse water jets at $r = 10$ and $10^3 \leq Re_j \leq 20 \times 10^3$ and studied the far-field ($50d$) concentration in detail. **Figure 11** shows that for the same velocity ratio, increasing the Reynolds number makes the mixed-fluid concentration more homogeneous. Such behavior is typical of passive scalar mixing and has also been observed in a variety of other flows (Dimotakis 2000). The spatial homogenization manifests itself in a preferred concentration (peak in the PDF), growing with increasing Reynolds number (**Figure 11**). Instantaneously, the concentration field is

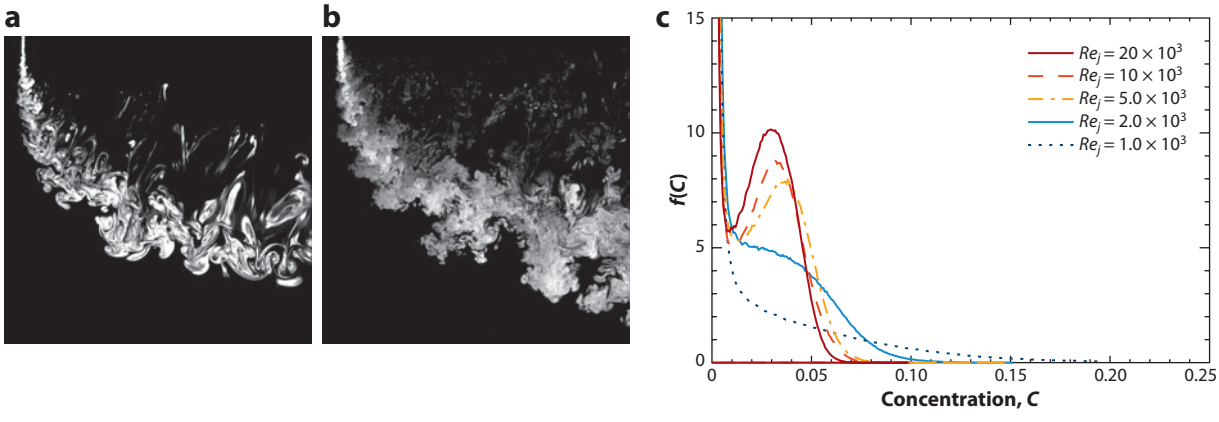

Figure 11

Mixed-fluid concentration in an $r = 32$ transverse jet at Re_j of (*a*) 10^3 and (*b*) 10^4. (*c*) The effect of Reynolds number on the probability density function of the mixed-fluid concentration in the far field. Figure taken from Shan & Dimotakis (2006).

intermittent, with regions of nearly constant concentration separated by fronts of large changes in concentration. Additionally, the concentration field is measured to be anisotropic at the smallest scales over the range of Reynolds numbers considered.

2.7. Nonequilibrium Nature of Flow and Modeling Implications

The turbulence in a transverse jet is three dimensional and anisotropic and in nonequilibrium. The budget of the turbulence kinetic energy $k = \langle u_i u_i/2 \rangle$ is described by its governing equation,

$$\frac{\partial}{\partial t}k + \underbrace{U_j \frac{\partial}{\partial x_j}k}_{\text{convection}} = \underbrace{-\langle u_i u_j \rangle \frac{\partial U_i}{\partial x_j}}_{\text{production}} \underbrace{- \nu \left\langle \frac{\partial u_i}{\partial x_j}\frac{\partial u_i}{\partial x_j} \right\rangle}_{\text{dissipation}}$$
$$\underbrace{- \frac{1}{2}\frac{\partial}{\partial x_j}\langle u_i u_i u_j \rangle}_{\text{turbulent transport}} + \underbrace{\nu \frac{\partial^2}{\partial x_j \partial x_j}k}_{\text{viscous diffusion}} \underbrace{- \frac{1}{\rho}\frac{\partial}{\partial x_i}\langle u_i p \rangle}_{\text{pressure transport}}. \quad (11)$$

Muppidi & Mahesh (2007) computed the various terms in the above budget from their DNS of an $r = 5.7$, $Re_j = 5{,}000$ jet. They found the production and dissipation terms to be generally dominant; however, the pressure transport term is generally nonnegligible and is dominant at some locations. Moreover, the relative values of terms at the jet exit differ significantly from those in a regular pipe flow. The ratio of the local rate of production of the turbulence kinetic energy to its local dissipation rate (P/ε) is a measure of the deviation from equilibrium. As shown in **Table 1**, P/ε in a transverse jet shows significant variability, has regions where it is much greater than 1, and is noticeably different from its values in a free jet or channel flow. The edges of the jet have P/ε values greater than 1.0, and P/ε is higher on the leading edge than at the trailing edge along the jet length. This suggests that the turbulence kinetic energy produced near the jet edges is transported toward the center of the jet at which $P/\varepsilon < 1.0$. The highest values of P/ε (over the entire domain) are observed at the leading edge of the jet at $s = rd$. This location corresponds to a significant change in the direction of the jet fluid. The relative locations of peak production and peak dissipation over the jet cross section display a sharp transition between the near and far fields (**Figure 12**). In the near field, the peak production is located at the windward side of the jet,

Table 1 P/ε **at select locations in an** $r = 5.7$, $Re_j = 5{,}000$ **transverse jet**

		P/ε
Upstream of jet exit	Near wall ($x/d = -0.46$)	1.916
	Pipe center	0.029
$s/rd = 0.1$	Leading edge	2.817
	Center streamline	0.0255
	Trailing edge	1.929
$s/rd = 1.0$	Leading edge	8.714
	Center streamline	0.650
	Trailing edge	1.883
$s/d = 15.0$	Center streamline	0.452
$s/d = 20.0$	Center streamline	0.483
Other flows	Regular jet ($r/r_{\frac{1}{2}} = 0.7$)	0.8
	Channel ($y^+ = 11.8$)	1.81

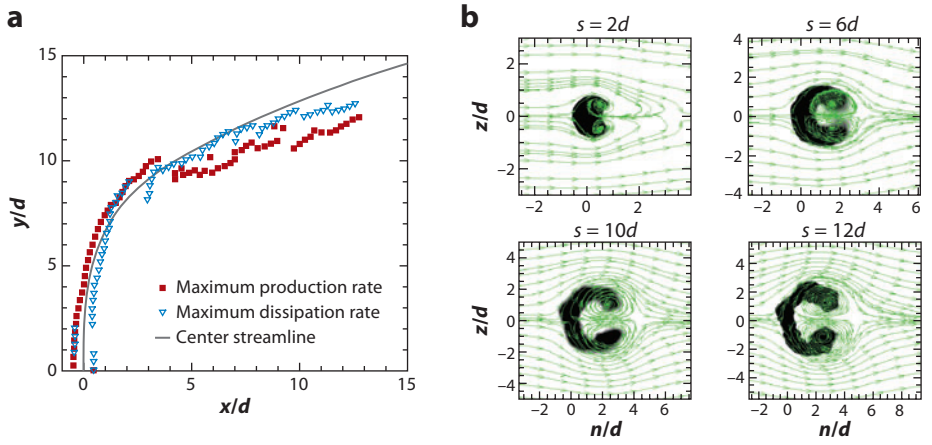

Figure 12

(*a*) Nature of the turbulence kinetic energy budget for an incompressible transverse jet, comparing the trajectory of the maximum production rate (*squares*) over the jet cross section with the trajectory of the maximum dissipation rate (*triangles*). The center streamline trajectory is represented by the solid line. (*b*) Evolution of a jet cross section at $s = 2d$, $6d$, $10d$, and $12d$. Figure taken from Muppidi & Mahesh (2007).

while the peak dissipation is located toward the leeward side. In contrast, in the far field, once the CVP has fully formed, the production is maximum on the leeward side of the jet, while the peak dissipation is located toward the windward side. This behavior is consistent with the upstream acceleration dominating the flow in the near field and CVP entrainment on the downstream side dominating the far field.

Such behavior poses challenges to time-averaged prediction methodologies. Hoda & Acharya (2000) conducted an extensive evaluation of several k-ε and k-ω models and concluded that existing models generally provide overly simplistic predictions of jets in crossflow. They found that the ε equation in k-ε models is inadequate in the jet region (which has large gradients in all directions) and suggested the need to optimize the ε budget, possibly using DNS. They noted that nonlinear models do not provide significantly better predictions than linear models, possibly because coefficients of the nonlinear models are obtained from simple wall-bounded flows. Additionally, Acharya et al. (2001) provided a detailed review of the application of Reynolds-averaged Navier-Stokes (RANS) models to film cooling. They noted that two equation models generally underpredict the lateral spread and mixing of the jet and overpredict the vertical penetration. The assumption of isotropic eddy viscosity is found inappropriate. Also Reynolds stress–transport model predictions are not substantially better than two-equation model predictions, despite modeling turbulence anisotropy. As seen in Muppidi & Mahesh's (2007) budget, the pressure transport term, which is mostly ignored or modeled along with turbulent transport (Pope 2000), is quite significant for transverse jets. The neglect or improper treatment of pressure transport is likely an additional source of error. The prediction of scalar mixing is even more challenging. **Figure 13** shows scatter plots of the eddy diffusivity computed by Muppidi & Mahesh (2008) from their DNS. Not only is the eddy diffusivity not isotropic, but there also are regions of countergradient diffusion.

There are also some numerical considerations. The flow (intensities, k, ε, budget terms) contains steep gradients at the jet edges in the near field. Grid convergence in the near field is therefore especially important. As noted in Section 2.3, interaction with the crossflow affects the flow inside

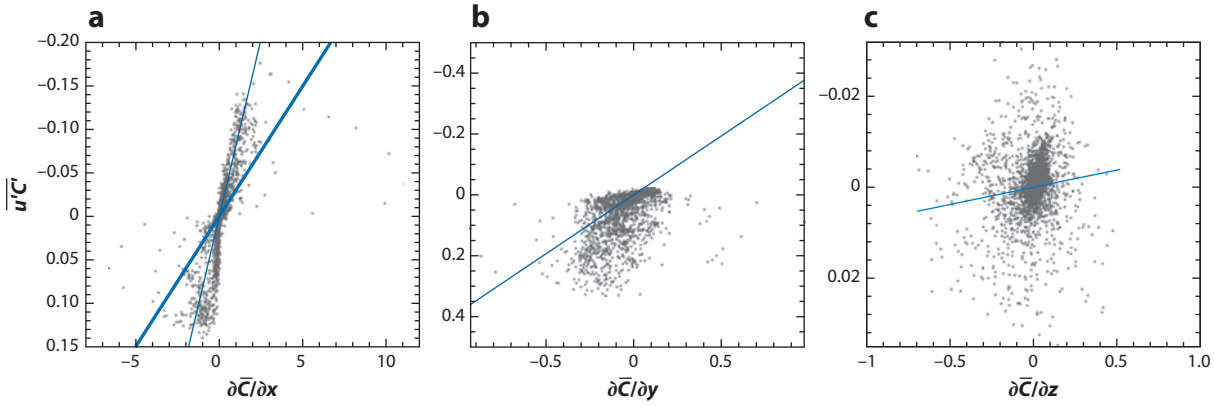

Figure 13

The dependence of turbulent scalar fluxes on the mean scalar gradient: (*a*) $\overline{u'C'}$ versus $\partial\bar{C}/\partial x$, (*b*) $\overline{v'C'}$ versus $\partial\bar{C}/\partial y$, and (*c*) $\overline{w'C'}$ versus $\partial\bar{C}/\partial z$. The thin lines show the least-squares fit for (*a*) D_{t1}, (*b*) D_{t2}, and (*c*) D_{t3}, respectively. The thick line in panel *a* shows the overall diffusivity D_t obtained by equating the measured and modeled production of the passive scalar variance. Figure taken from Muppidi & Mahesh (2008).

the pipe/nozzle. Inclusion of the pipe/nozzle is therefore necessary for any transverse jet simulation (RANS, LES, or DNS), especially at low-velocity ratios. Film cooling in particular is known to depend on both pipe and plenum geometry (e.g., Peterson & Plesniak 2004). Moreover, the budgets at the jet exit differ considerably from their values for a turbulent pipe. Therefore, computations that do not include the pipe would have to prescribe fairly complex boundary conditions at the jet exit.

2.8. Stability

In Section 2.3 we discuss the shear-layer vortices that form on the windward side of the jet. Recent studies indicate that at jet-to-crossflow velocity ratios below 3–4, the onset of the shear-layer instability is driven by mechanisms that may be different from the typical Kelvin-Helmholtz instability. Camussi et al. (2002) showed that for this range of velocity ratios, there is a very strong oscillation or waving in the flow, leading to "large scale, periodic" shear-layer rollup. The experiments of Megerian et al. (2007) and Davitian et al. (2010) explore the range $1.15 \leq r < \infty$, at fixed jet Reynolds numbers (2,000 and 3,000). For $\infty > r > 3.2$, dominant shear-layer instabilities are observed through measured spectra to be strengthened, to move closer to the jet orifice, and to increase in frequency as the crossflow velocity U_∞ increases for a fixed jet Reynolds number.

Figure 14 shows sample results for the evolving spectral characteristics along the jet shear layer (location along the jet trajectory denoted by s/d). The shear-layer instabilities at higher r values (above 3.2) exhibit downstream frequency shifting along the jet shear layer for $r = 4.1$ (**Figure 14*b***). When r is reduced below approximately 3.2, single frequency instabilities are dramatically strengthened, forming almost immediately beyond the jet exit within the shear layer, without any evidence of frequency shifting (**Figure 14*c***). The spectra in **Figure 14*a*,*b*** are typical of convectively unstable shear layers for which disturbances grow downstream of their initiation (Huerre & Monkewitz 1990). In contrast, the spectra in **Figure 14*c*** are typical of an absolutely unstable shear flow for which disturbances also grow near their location of initiation. As a result, the flow becomes self-excited. From a control standpoint, the transition affects the transverse

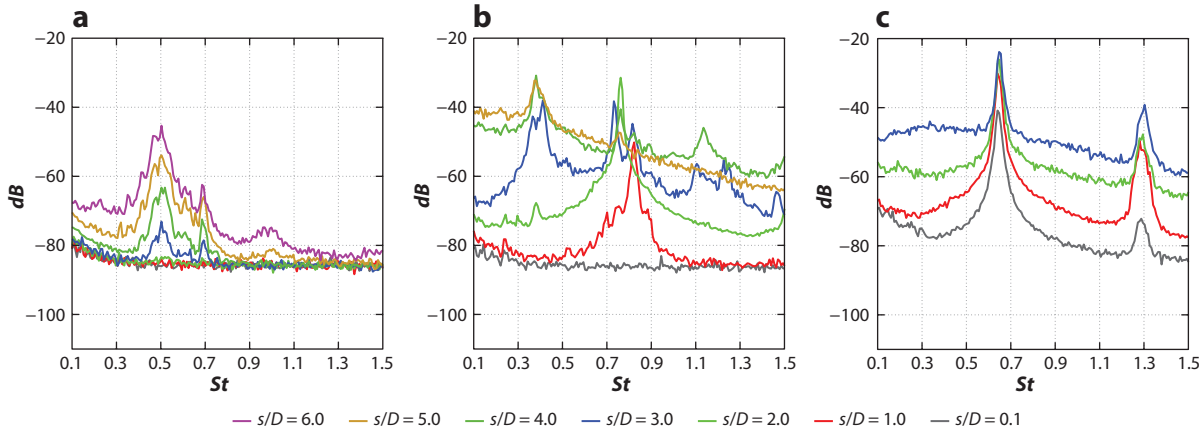

Figure 14

The nature of upstream shear-layer instabilities reflected in velocity spectra in the windward shear layer for an $Re_j = 2{,}000$ transverse jet: (*a*) free jet, (*b*) $r = 4.1$, and (*c*) $r = 2.0$. Figure taken from Megerian et al. (2007).

jet's response to small-amplitude forcing. As shown by Megerian et al. (2007), when the jet is axisymmetrically forced at 1% of the mean velocity, the forcing frequency takes over the spectral character of the shear layer when $r > 3.2$, but it has little effect when $r < 3.2$ and the flow is globally unstable. The globally unstable regime appears not to be very responsive to low-to-moderate flow excitation; it only responds to strong square wave forcing.

De B. Alves et al. (2008) performed linear stability analysis on a modified version of Coelho & Hunt's (1989) solution for $4 \leq r \leq 10$. Their analysis predicts that the most unstable mode is axisymmetric and that the Strouhal number decreases with increasing r, in agreement with experiment. In a linear stability analysis of an $r = 3$ transverse jet, Bagheri et al. (2009) considered a base flow that was steady, obtained by selectively damping certain frequencies. The jet was prescribed to be parabolic at the inflow, and the steady solution had a CVP and horseshoe vortices near the wall. The analysis revealed higher-frequency unstable global eigenmodes associated with shear-layer instabilities on the CVP and lower-frequency modes associated with shedding vortices in the wake of the jet (**Figure 15**).

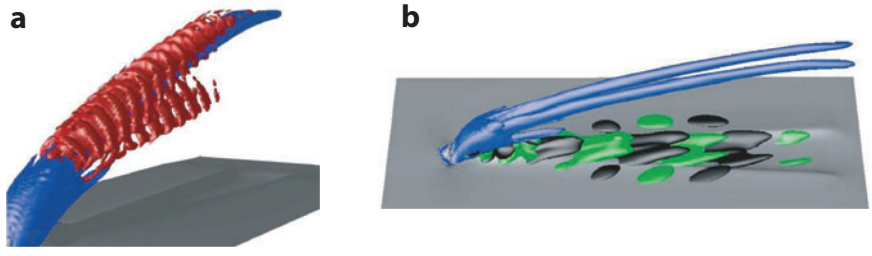

Figure 15

Modes from the stability analysis of Bagheri et al. (2009). (*a*) High-frequency modes (λ_2 isocontour in *red*) along with the base flow (λ_2 isocontour in *blue* and u contours in *gray*). (*b*) Low-frequency spanwise velocity near the wall (*green* and *black* correspond to negative and positive velocities, respectively) along with the base flow as in panel *a*.

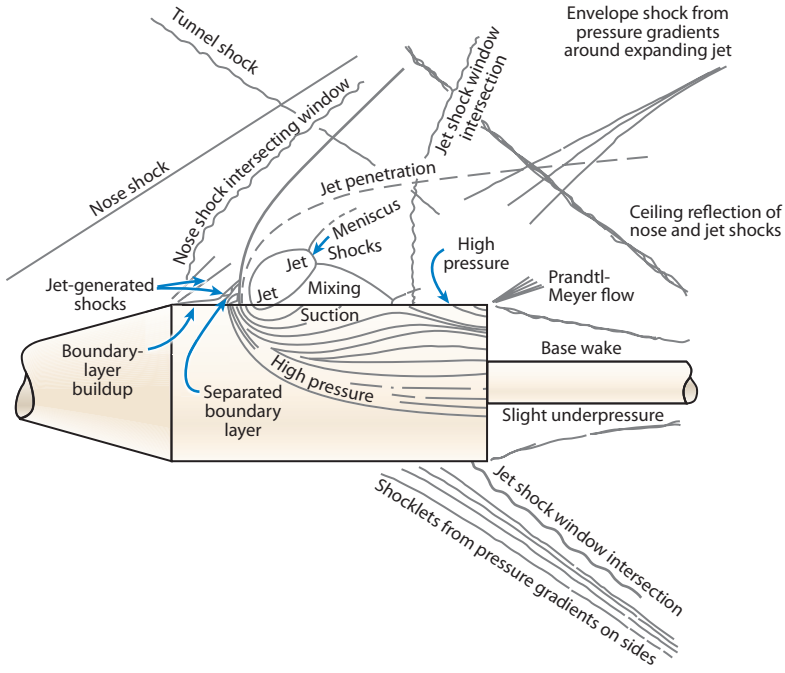

Figure 16

Schematic of the flow field in the interaction of a supersonic jet with a supersonic crossflow. Figure taken from Morkovin et al. (1952).

3. COMPRESSIBLE JETS IN CROSSFLOW

3.1. Overview

Early studies of high-speed jets in crossflow mostly considered applications to thrust vectoring, whereas most recent studies consider scramjet combustors. Visualization remains an important component of experimental studies. Most computations have used the RANS methodology, and there have been several recent LES or hybrid RANS-LES simulations. Experiments at high speeds are not as common as those at low speeds, particularly if turbulence or mixing data are to be measured; quantitative data are hard to acquire at high velocities.

A fairly detailed qualitative description of the flow, especially from a gasdynamical perspective, is available from some early studies. For example, **Figure 16** shows a sketch of the flow field described by Morkovin et al. (1952) based on their schlieren visualization and surface-pressure measurements of the flow induced by supersonic injection from a cone-cylinder configuration into a Mach 1.9 crossflow. Such work examined the surface-pressure field and the resulting forces and moments induced by the transverse jet. The experiments of Zukoski & Spaid (1964) show the importance of the ratio of stagnation pressure in the jet to the free-stream value on scaling jet penetration. Extensive experimental and modeling studies were performed by Schetz, Billig, and coworkers (e.g., Orth et al. 1969, Schetz & Billig 1987) to examine the effect of underexpanded versus perfectly expanded jets, injection angle, and multiple jets. The sophistication of the measurements has increased. However, fewer quantitative data are available compared to those for low-speed flows. Velocity measurements of a jet interacting with supersonic crossflow have been performed using laser Doppler velocimetry for a sonic jet (Santiago & Dutton 1997), hot-film anemometry for an

angled supersonic jet (McCann & Bowersox 1996), and particle image velocimetry for a jet issuing from a missile half-body (Mahmud & Bowersox 2003). Jet penetration into a supersonic flow has been measured using schlieren imaging (Papamoschou & Hubbard 1993, Ben-Yakar et al. 2006), concentration measurements of differing fluids (Orth & Funk 1967, Fuller et al. 1992), planar Mie scattering (Gruber et al. 1997a,b), and laser-induced fluorescence (McDaniel & Graves 1988, Hollo et al. 1994, McMillin et al. 1994, Ben-Yakar et al. 2006). A series of experiments by Beresh et al. (2005a,b, 2006) provides detailed streamwise and crossplane PIV data for supersonic jets issuing into subsonic crossflow. These more detailed measurements have enabled insight into the overall structure of transverse jets and their penetration and mixing properties. Some experiments have also explored the dependence of the flow on many possible parameters (e.g., Papamoschou & Hubbard 1993, Gruber et al. 1997b, Ben-Yakar et al. 2006).

Most computations of high-speed injection flow fields have used algebraic mixing-length and eddy-viscosity models. Chenault et al. (1999) noted that such models can yield estimates of the overall flow structure but cannot correctly model secondary flows or turbulent stresses associated with the injection. They evaluated a Reynolds-stress transport model, which yields significantly better results. There have been several LES and hybrid RANS-LES simulations of underexpanded sonic jets (e.g., Peterson et al. 2006, Kawai & Lele 2009, Génin & Menon 2010, Boles et al. 2010, Chai & Mahesh 2011, Ferrante et al. 2011), most of which evaluate their particular numerical method or subgrid model for this class of problems.

3.2. Qualitative Time-Averaged Behavior

Here we consider two regimes. The first (**Figure 17*a*,*c***) has a sonic jet interacting with a supersonic free-stream flow, as is the case in scramjet combustors. The second regime has a supersonic jet interacting with a subsonic crossflow (**Figure 18*a***), as occurs in thrust vector control applications. **Figures 17** and **18** are from the LES of Chai & Mahesh (2011) performed under conditions corresponding to the experiments of Santiago & Dutton (1997) and Beresh et al. (2005a,b, 2006), respectively.

Figure 17*a* shows contours of the mean Mach number on the symmetry plane and a near-wall plane parallel to the wall, with the free-stream Mach number $M_\infty = 1.6$, the Reynolds number based on the free-stream velocity and jet diameter $Re_j = 2.4 \times 10^5$, the density and pressure ratio between the nozzle chamber and crossflow $\rho_{0j}/\rho_\infty = 5.5$ and $p_{0j}/p_\infty = 8.4$, and the jet-to-crossflow momentum flux ratio $J = 1.7$ (Santiago & Dutton 1997). **Figure 17*c*** shows the corresponding crossplane contours of the Mach number and pressure contours parallel to the wall. Similar to the behavior displayed by incompressible jets in crossflow, the upstream boundary layer separates to form a horseshoe vortex. There exists a near-field pressure gradient in the streamwise direction, and the jet bends in the direction of the free stream in the near field and forms a CVP in the far field. Moreover, the crossflow accelerates around the jet, and a saddle node is observed on the symmetry plane. There also are significant differences from incompressible transverse jets. A bow shock is observed ahead of the jet, barrel shocks are observed at its periphery, and the jet fluid forms a Mach disk as it expands into and bends toward the crossflow. The pressure gradient at the jet exit makes it difficult to precisely define the extent to which the jet is underexpanded. The wall pressure displays the footprint of the bow shock. Additionally, as the crossflow accelerates around the jet, it can become supersonic. **Figure 18*a*** shows contours of the mean Mach number when $M_\infty = 0.8$; $M_j = 3.73$; $J = 10.2$; the density, pressure, and temperature ratio between the nozzle chamber and crossflow $\rho_{0j}/\rho_\infty = 47.1$, $p_{0j}/p_\infty = 49.1$, and $T_{0j}/T_\infty = 1.05$; and $Re_j = 1.9 \times 10^5$ (Beresh et al. 2006). Here the flow shows an even stronger resemblance to incompressible transverse jets, with one important difference being the shock cells that are observed within the jet.

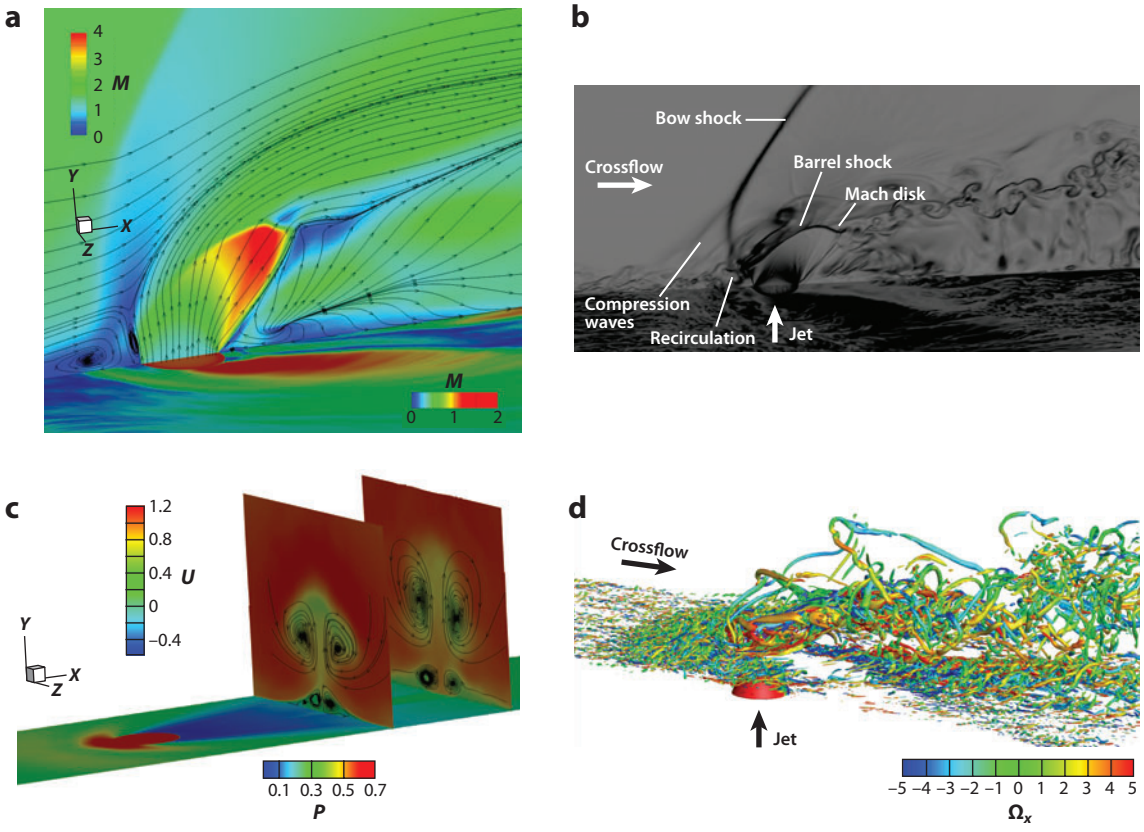

Figure 17

Mean and instantaneous flow in the interaction of a sonic jet with Mach 1.6 crossflow. (*a*) Mean Mach number (*M*) contours on central and horizontal planes (with different contour levels). (*b*) Instantaneous density-gradient magnitude on symmetry and wall-parallel planes. (*c*) Mean streamwise velocity contours on two downstream crossplanes and the mean pressure contour on the horizontal plane. (*d*) Isosurface of the second invariant of the velocity-gradient tensor colored by the streamwise vorticity. Figure taken from Chai & Mahesh (2011).

3.3. Qualitative Instantaneous Behavior

The mean flow conceals fairly complex instantaneous behavior. Let us consider the sonic jet interacting with a Mach 1.6 crossflow (**Figure 17*b*,*d***). The density-gradient contours show how the crossflow turbulent boundary layer decelerates in response to the jet and forms a bow shock. The adverse pressure gradient induces separation, which in turn yields a family of compression waves in front of the jet. Upon exiting the orifice, the sonic jet tries to penetrate and expand into the crossflow and in the process forms an inclined barrel shock and Mach disk. The shear layer on the windward side of the jet rolls up, similar to its behavior at low speeds. The barrel shock and Mach disk are quite unsteady. The unsteadiness of the barrel shock appears to be related to acoustic waves propagating across the jet exit (e.g., Kawai & Lele 2009, Génin & Menon 2010). The Mach disk unsteadiness is such that a significant portion of the high-velocity jet fluid bypasses the upstream edge of the Mach disk during certain instants (VanLerberghe et al. 2000). This results in high shear downstream of the Mach disk and prominent large-scale coherent vortices (**Figure 18**). Such vortices are not observed in subsonic crossflow.

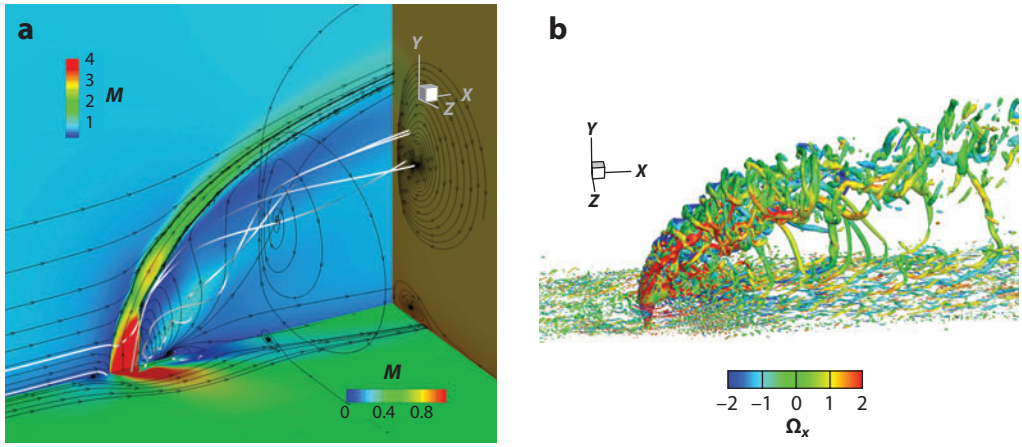

Figure 18

Mean and instantaneous flow for a supersonic jet interacting with subsonic crossflow: (*a*) mean Mach number (*M*) and (*b*) isosurface of the second invariant of the velocity-gradient tensor colored by the streamwise vorticity. Figure taken from Chai & Mahesh (2011).

Figure 17*d* visualizes instantaneous vortical structures using the second invariant of the velocity-gradient tensor. The range of scales of motion is apparent. Moreover, the region downstream of the jet shows irrotational regions on either side of the jet. These regions correspond to the expansion and acceleration of the crossflow around the jet and also possess large density gradients (the horizontal plane in **Figure 18*b***). The jet plume has a complex structure with streamwise vorticity of different signs on either side of the symmetry plane. With time-averaging, this yields a CVP. Incompressible transverse jets (Section 2.3) can separate inside the nozzle/pipe at low *r*. Such behavior has generally not been discussed for high-speed jets, an exception being Beresh et al. (2003), who noted how supersonic jets issuing into subsonic crossflow can separate inside the nozzle at low *J*, affecting the near-field shock waves and the thrust vector as a result.

3.4. Jet Trajectory

The trajectory of incompressible transverse jets is most commonly scaled with *rd*, as discussed in Section 2.4. For fluids of different density, *r* is related to the momentum flux ratio, $J = \rho_j U_j^2 / \rho_\infty U_\infty^2$. At high-enough speeds that compressibility becomes important, jet penetration and trajectory can also depend on

$$\frac{p_j}{p_\infty}, \frac{\rho_j}{\rho_\infty}, \frac{T_j}{T_\infty}; \text{ molecular weights } M_{wj} \text{ and } M_{w\infty}; \text{ and Mach numbers } M_j \text{ and } M_\infty.$$

In addition, the crossflow boundary layer, jet velocity profile, and orifice shape can also be important. Given this fairly large parameter space, it is perhaps not surprising that a variety of correlations and observations exist on jet penetration and trajectory. Most empirical correlations are based on visualization of the flow. Additionally, most correlations are for cases in which the crossflow is supersonic. Different metrics to assess the jet penetration have been used. Early studies employing schlieren imaging used the height of the Mach disk as a measure (e.g., Zukoski & Spaid 1964; Schetz et al. 1967, 1968; Hersch et al. 1970), whereas subsequent studies have used measures such as the visually observable upper edge of the jet from schlieren images (Ben-Yakar et al. 2006), the edge of the fluorescing plume at which the injectant mole fraction is approximately 1%

(McDaniel & Graves 1988), and the intensity of planar Rayleigh scattering images corresponding to 90% of the average intensity behind the bow shock.

The momentum ratio J is equal to $\gamma_j p_j M_j^2/\gamma_\infty p_\infty M_\infty^2$. Moreover, for supersonic crossflow, the near-field crossflow pressure is that after the bow shock (denote by $p_{\infty 2}$). The Rankine-Hugoniot equations yield

$$\frac{p_{\infty 2}}{p_\infty} = \frac{2\gamma_\infty}{\gamma_\infty + 1} M_\infty^2 - \frac{\gamma_\infty - 1}{\gamma_\infty + 1}, \tag{12}$$

which allows J to be expressed as

$$J = \frac{\gamma_j}{\gamma_\infty} \frac{p_j}{p_{\infty 2}} M_j^2 \frac{2\gamma_\infty}{\gamma_\infty + 1} - \frac{\gamma_\infty - 1}{M_\infty^2(\gamma_\infty + 1)}. \tag{13}$$

The crossflow Mach number therefore influences J by determining the pressure behind the bow shock. As noted by Papamoschou & Hubbard (1993), if $p_j/p_{\infty 2}$ is held fixed, J depends most strongly on M_j, while M_∞ has a much smaller effect. In the absence of crossflow, the jet-exit pressure determines the extent to which it is under-/overexpanded. Conversely, for a transverse jet, varying the exit pressure also varies the momentum flux ratio. If J is held constant and the exit pressure is varied, the jet Mach number has to be correspondingly varied. This makes assessing the effect of the exit pressure solely in terms of its effect on jet expansion difficult.

An insightful estimate of the jet trajectory was performed by Schetz & Billig (1966), who considered the forces acting on a slug of jet fluid, away from shock waves. An approximate force balance along and normal to the jet axis yielded an equation for the angle $\alpha(s)$ made by the jet trajectory s with the horizontal direction (assuming vertical injection):

$$\frac{d\alpha}{ds} = -\frac{C_D h(\alpha) \rho_\infty U_\infty^2 \sin^2 \alpha}{2\rho_j U_j^2 [A_j^2/A(s)][\rho_j/\rho(s)]}. \tag{14}$$

Here $h(s)$ denotes the jet width, C_D a drag coefficient, $A(s)$ the local cross-sectional area, and $\rho(s)$ the local jet density. The subscript j denotes quantities at the jet exit. Schetz & Billig used empirical expressions for h and C_d, an assumption of an elliptical cross section of prescribed ellipticity to obtain A, and a constant value for ρ to integrate the above equation to obtain the jet trajectory. Comparison to subsonic crossflow data in the near field (up to $4d$) showed good agreement for $J = 4.75$ and significant overprediction for $J = 16.35$. Despite the disagreement, the analysis is valuable, in particular for its intuitively appealing notion of effective back pressure to represent the complex pressure field at the jet exit. The effective back pressure allows underexpanded jets to be considered; it determines the height of the first Mach disk, beyond which Equation 14 for the trajectory is applied.

Much experimental data have been gathered over the past few decades, and several correlations for jet trajectory have been proposed as a result. As seen from **Table 2**, the correlations either are a power law or involve a logarithmic fit, and even correlations with similar functional form can have

Table 2 A compilation of correlations for the trajectories of high-speed jets

	Trajectory
Gruber et al. (1997b)	$\frac{y}{dJ} = 1.20(\frac{x+d/2}{dJ})^{0.344}$
McDaniel & Graves (1988)	$\frac{y}{d} = \frac{0.344}{M_\infty^2} \frac{p_j}{p_\infty} \ln[2.077(x/d + 2.059)]$
Rothstein & Wantuck (1992)	$\frac{y}{d} = 2.173\, J^{0.276}(x/d)^{0.281}$
	$\frac{y}{d} = J^{0.312} \ln[4.704(x/d + 0.637)]$
Vranos & Nolan (1965)	$\frac{y}{d} = 1.68\, J^{0.5}(x/d)^{0.0866}$
Rogers (1971)	$\frac{y}{d} = 3.87\, J^{0.3}(x/d)^{0.143}$

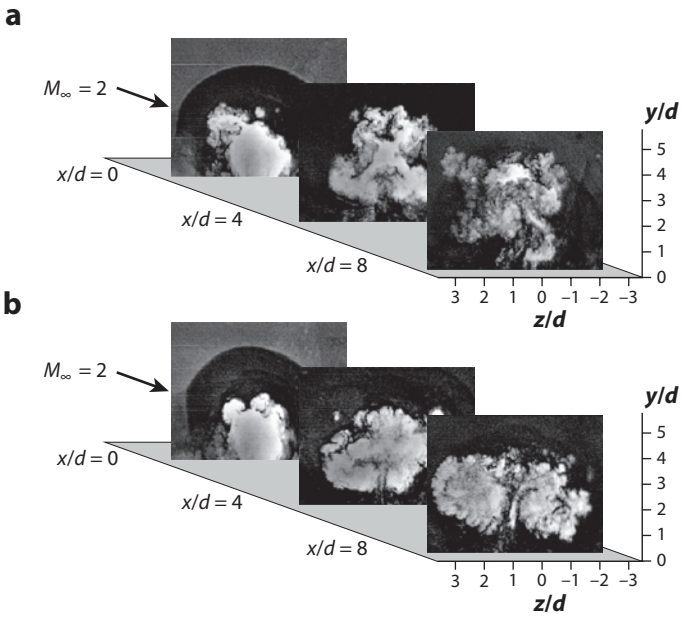

Figure 19

Instantaneous end views from Gruber et al.'s experiments illustrating the difference between (*a*) air and (*b*) helium jets. Figure reprinted with permission from Gruber et al. (1997b). Copyright 1997, American Institute of Physics.

significantly different constants. There is experimental evidence that parameters other than J can be important. Papamoschou & Hubbard (1993) considered helium jets in crossflowing air at Mach 2 to 3 and performed several experiments in which they varied J, M_j, and the jet pressure and density ratios. Defining jet penetration visually from schlieren images, they concluded that penetration strongly depends on the momentum ratio and depends less on the free-stream Mach number, jet Mach number, pressure ratio, and density ratio. The experiments of Gruber et al. (1997b) use planar Rayleigh scattering to study sonic helium and air jets with the same momentum flux ratio issuing into the same crossflow. They found that the difference in molecular weight does not affect the penetration; however, the dynamics of the large-scale structures is quite different. The large-scale motions were observed to break down in the air jet, whereas the helium jet stayed more coherent over longer distances (**Figure 19**). The authors explained this behavior by noting that an appropriate convective Mach number was three times larger for helium than for air. Another study by Ben-Yakar et al. (2006) used schlieren and OH planar laser-induced fluorescence to contrast sonic hydrogen and ethylene jets with the same momentum ratio. Similar to Gruber et al., the lighter, and therefore faster, hydrogen jet stayed coherent for longer distances. However, in contrast to Gruber et al., who did not find significant differences in penetration between jets of different molecular weights, Ben-Yakar et al. found that the ethylene jet penetrated more. They attributed this behavior to the ethylene jet having lower velocities for the same J, which induces the coherent motions on the windward side to tilt in the crossflow direction, lose their coherence, and mix more.

3.5. Mixing

As discussed in Section 2.6, the near-field mixing of incompressible transverse jets as reflected by scalar PDFs is different from that in the far field. This difference is likely greater in

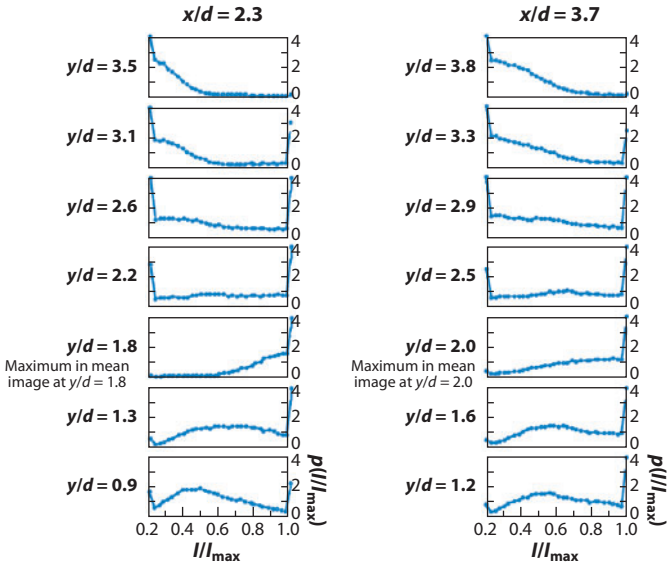

Figure 20

Scalar probability density functions of an underexpanded sonic jet injected into Mach 1.6 crossflow from VanLerberghe et al. (2000).

high-speed jets. The experiments of VanLerberghe et al. (2000) used planar laser-induced fluorescence from acetone molecules to study mixing in an underexpanded sonic jet injected into a Mach 1.6 crossflow. The authors used instantaneous images to extract PDFs of the image intensity to quantify mixing, as well as to develop a qualitative description of the entrainment process. The large coherent motions discussed in Section 3.3, along with mushroom-shaped plumes issuing out of the jet boundary, were observed to entrain large amounts of free-stream fluid. As a result, mean concentrations were intermediate to their pure jet and crossflow values. However, the PDFs indicated large regions of unmixed fluid. As seen from **Figure 20**, the most near-field mixing was observed in the center of the wake region slightly below the jet centerline. Also the level of mixing improved with downstream distance from the Mach disk, as the flow evolved into the CVP. Entrainment of crossflow fluid by large windward coherent motions was also observed by Ben-Yakar et al. (2006), who contrasted sonic hydrogen and ethylene jets with the same momentum ratio in a Mach 3.38 crossflow. Visually defining coherent motions, they constructed *x-t* diagrams from which they extracted convection velocities and inclination angles. Such analysis allowed estimation of the directional shear experienced by the coherent motions, which they found important in the ethylene jets losing their coherence and mixing more with the crossflow.

4. SUMMARY

This article reviews our fundamental understanding of single-phase, nonreacting transverse jets in incompressible and compressible regimes. As expected, more quantitative information is available at low speeds owing to the difficulties in performing experiments and turbulent simulations at high speeds. Much attention has been devoted to qualitative flow structure, and there is a general consensus on the important elements. Perhaps the impact of low-velocity ratios on the flow structure is less appreciated. It is known that different definitions of the jet trajectory yield different answers and that scaling of similarly defined jet trajectories is not straightforward. The widely

used *rd* scaling has sound support in the far field, but has less in the near field, whose behavior affects the overall far-field penetration. The parameter space at high speeds is fairly large, and even experimentally derived correlations for trajectories show significant scatter. Transverse jets entrain free-stream fluid at higher rates than regular jets. This behavior not only is displayed when the CVP is fully formed, but is also observed in the near field, in which the jet fluid is strongly accelerated. In contrast to a regular jet, the near field of a transverse jet experiences strong pressure gradients in the crossflow direction. Higher pressures at the windward side of the jet also induce separation inside the jet nozzle/pipe at low-velocity ratios. Studies at low speeds show that mixing depends more on Reynolds number than jet trajectory or spatial extent does. Moreover, the PDFs of scalar concentrations in the near field are qualitatively different from those in the far field. Along with visualizations, PDFs measured in high-speed flow show that coherent motions entrain large amounts of crossflow fluid, but mixing in the near field is not very effective. Turbulence kinetic energy budgets from DNS at low speeds reveal a flow that is highly anisotropic and in nonequilibrium. The ratios of production to dissipation vary widely, and there even are regions in which pressure transport is significant. Scalar transport is not well described by an isotropic eddy viscosity and even displays countergradient diffusion. Such behavior makes prediction using Reynolds-averaged methodologies difficult. Low-speed transverse jets appear globally unstable at low-velocity ratios, which suggests an intriguing pathway for their control.

DISCLOSURE STATEMENT

The author is not aware of any biases that might be perceived as affecting the objectivity of this review.

ACKNOWLEDGMENTS

I am grateful to Dr. Suman Muppidi and Mr. Xiaochuan Chai for many useful discussions during the course of preparing this review. I am extremely thankful to the NSF, AFOSR, and ONR for support.

LITERATURE CITED

Acarlar MS, Smith CR. 1987. A study of hairpin vortices in a laminar boundary layer. Part 2. Hairpin vortices generated by fluid injection. *J. Fluid Mech.* 175:43–83

Acharya S, Tyagi M, Hoda A. 2001. Flow and heat transfer predictions for film-cooling. *Ann. N.Y. Acad. Sci.* 934:110–25

Andreopoulos J, Rodi W. 1984. Experimental investigation of jets in cross-flow. *J. Fluid Mech.* 138:93–127

Babu PC, Mahesh K. 2004. Upstream entrainment in numerical simulations of spatially evolving round jets. *Phys. Fluids* 16:3699–705

Bagheri S, Schlatter P, Schmid PJ, Henningson DS. 2009. Global stability of a jet in crossflow. *J. Fluid Mech.* 624:33–44

Ben-Yakar A, Mungal MG, Hanson RK. 2006. Time evolution and mixing characteristics of hydrogen and ethylene transverse jets in supersonic crossflows. *Phys. Fluids* 18:026101

Beresh SJ, Henfling JF, Erven RJ. 2003. Flow separation inside a supersonic nozzle exhausting into a subsonic compressible crossflow. *J. Propuls. Power* 19:655–62

Beresh SJ, Henfling JF, Erven RJ, Spillers RW. 2005a. Penetration of a transverse supersonic jet into a subsonic compressible crossflow. *AIAA J.* 43:379–89

Beresh SJ, Henfling JF, Erven RJ, Spillers RW. 2005b. Turbulent characteristics of a transverse supersonic jet in a subsonic compressible crossflow. *AIAA J.* 43:2385–94

Beresh SJ, Henfling JF, Erven RJ, Spillers RW. 2006. Crossplane velocimetry of a transverse supersonic jet in a transonic crossflow. *AIAA J.* 44:3051–61
Boles JA, Edwards JR, Baurle RA. 2010. Large-eddy/Reynolds-averaged Navier-Stokes simulations of sonic injection into Mach 2 crossflow. *AIAA J.* 48:1444–56
Bosanquet CH, Pearson JL. 1936. The spread of smoke and gases from chimneys. *Trans. Faraday Soc.* 32:1249–63
Broadwell JE, Breidenthal RE. 1984. Structure and mixing of a transverse jet in incompressible flow. *J. Fluid Mech.* 148:405–12
Camussi R, Guj G, Stella A. 2002. Experimental study of a jet in a crossflow at very low Reynolds number. *J. Fluid Mech.* 454:113–44
Chai X, Mahesh K. 2011. *Simulations of high speed turbulent jets in cross flows*. Presented at AIAA Aerosp. Sci. Mett. New Horiz. Forum Aerosp. Expo., 49th, Orlando, FL, AIAA Pap. 2011-650
Chenault CF, Beran PS, Bowersox RDW. 1999. Numerical investigation of supersonic injection using a Reynolds-stress turbulence model. *AIAA J.* 37:1257–69
Chochua G, Shyy W, Thakur S, Brankovic A, Lienau K, et al. 2000. A computational and experimental investigation of turbulent jet and crossflow interaction. *Numer. Heat Transf. A* 38:557–72
Coelho SLV, Hunt JCR. 1989. The dynamics of the near field of strong jets in cross-flow. *J. Fluid Mech.* 200:95–120
Cortelezzi L, Karagozian AR. 2001. On the formation of the counter-rotating vortex pair in transverse jets. *J. Fluid. Mech.* 446:347–74
Crabb D, Durao DFG, Whitelaw JH. 1981. A round jet normal to a cross-flow. *Trans. ASME J. Fluids Eng.* 103:142–53
Davitian J, Getsinger D, Hendrickson C, Karagozian AR. 2010. Transition to global instability in transverse jet shear layers. *J. Fluid Mech.* 661:294–315
de B. Alves LS, Kelly RE, Karagozian AR. 2008. Transverse-jet shear-layer instabilities. Part 2. Linear analysis for large jet-to-crossflow velocity ratio. *J. Fluid Mech.* 602:383–401
Delavan SK, Webster DR. 2011. Unsteadiness of bivalve clam jet flow according to environmental conditions. *Aquat. Biol.* 13:175–91
Dimotakis PE. 2000. Mixing transition in turbulent flows. *J. Fluid Mech.* 409:69–98
Fearn RL, Weston RP. 1974. Vorticity associated with a jet in crossflow. *AIAA J.* 12:1666–71
Ferrante A, Matheou G, Dimotakis PE. 2011. LES of an inclined sonic jet into a turbulent crossflow at Mach 3.6. *J. Turbul.* 12(2):1–32
Foust J, Rockwell D. 2006. Structure of the jet from a generic catheter tip. *Exp. Fluids* 41:543–58
Fric TF, Roshko A. 1994. Vortical structure in the wake of a transverse jet. *J. Fluid Mech.* 279:1–47
Fuller EJ, Mays RB, Thomas RH, Schetz JA. 1992. Mixing studies of helium in air at high supersonic speeds. *AIAA J.* 30:2234–43
Gardner JE, Burgisser A, Stelling P. 2007. Eruption and deposition of the Fisher Tuff (Alaska): evidence for the evolution of pyroclastic flows. *J. Geol.* 115:417–36
Génin F, Menon S. 2010. Dynamics of sonic jet injection into supersonic crossflow. *J. Turbul.* 11:1–13
Gogineni S, Rivir R, Pestian D, Goss L. 1996. High free-stream turbulence influence on turbine film-cooling flows. *Phys. Fluids* 8(9):S4
Gopalan S, Abraham BM, Katz J. 2004. The structure of a jet in cross flow at low velocity ratios. *Phys. Fluids* 16:2067–87
Gruber MR, Nejad AS, Chen TH, Dutton JC. 1997a. Large structure convection velocity measurements in compressible transverse injection flowfields. *Exp. Fluids* 12:397–407
Gruber MR, Nejad AS, Chen TH, Dutton JC. 1997b. Compressibility effects in supersonic transverse injection flowfields. *Phys. Fluids* 9:1448–61
Gutmark EJ, Ibrahim IM, Murugappan S. 2008. Circular and noncircular subsonic jets in cross flow. *Phys. Fluids* 20:075110
Han D, Mungal MG. 2001. Direct measurement of entrainment in reacting/nonreacting turbulent jets. *Combust. Flame* 124:370–86
Hasselbrink EF, Mungal MG. 2001. Transverse jets and jet flames. Part 1. Scaling laws for strong transverse jets. *J. Fluid Mech.* 443:1–25

Haven BA, Kurosaka M. 1997. Kidney and anti-kidney vortices in crossflow jets. *J. Fluid Mech.* 352:27–64
Hersch M, Povinelli LA, Povinelli FP. 1970. Optical study of sonic and supersonic jet penetration from a flat plate into a Mach 2 airstream. *NASA TN D-5717*, Glenn Res. Cent., Cleveland
Hoda A, Acharya S. 2000. Predictions of a film coolant jet in crossflow with different turbulent models. *J. Turbomach.* 122:558–69
Hollo SD, McDaniel JC, Hartfield RJ. 1994. Quantitative investigation of compressible mixing: staged transverse injection into Mach 2 flow. *AIAA J.* 32:528–34
Huerre P, Monkewitz PA. 1990. Local and global instabilities in spatially developing flows. *Annu. Rev. Fluid Mech.* 22:473–537
Iourokina IV, Lele SK. 2006. Large eddy simulation of film cooling above a flat plate from inclined cylindrical holes. *ASME Conf. Proc. Symp. Adv. Numer. Model. Aerodyn. Hydrodyn. Turbomach.*, Pap. FEDSM2006-98282. New York: ASME
Kamotani Y, Greber I. 1972. Experiments on turbulent jet in a crossflow. *AIAA J.* 10:1425–29
Karagozian AR. 1986. An analytical model for the vorticity associated with a transverse jet. *AIAA J.* 24:429–36
Kawai S, Lele SK. 2009. Dynamics and mixing of a sonic jet in a supersonic turbulent crossflow. In *Center for Turbulence Research Annual Research Briefs*, pp. 285–98. Stanford, CA: Cent. Turbul. Res.
Keffer JF, Baines WD. 1963. The round turbulent jet in a cross-wind. *J. Fluid Mech.* 15:481–96
Kelso RM, Lim TT, Perry AE. 1996. An experimental study of round jets in cross-flow. *J. Fluid Mech.* 306:111–44
Kelso RM, Smits AJ. 1995. Horseshoe vortex systems resulting from the interaction of a laminar boundary layer and a transverse jet. *Phys. Fluids* 7:153–58
Krothapalli A, Lourenco L, Buchlin JM. 1990. Separated flow upstream of a jet in cross-flow. *AIAA J.* 28:414–20
Liscinsky DS, True B, Holdeman JD. 1995. Crossflow mixing of noncircular jets. *J. Propuls. Power* 12:225–30
Mahesh K, Constantinescu G, Moin P. 2004. A numerical method for large-eddy simulation in complex geometries. *J. Comput. Phys.* 197:215–40
Mahmud Z, Bowersox R. 2003. *Supersonic missile body jet interaction flowfields at low momentum-parameter-ratio*. Presented at Aerosp. Sci. Meet. Exhib., 41st, Reno, NV, AIAA Pap. 2003-1244
Margason RJ. 1993. Fifty years of jet in cross flow research. *Comput. Exp. Assess. Jets Cross Flow*, *AGARD-CP 534*, Advis. Group Aeronaut. Res. Dev., Washington, DC
Marzouk YM, Ghoniem AF. 2007. Vorticity structure and evolution in a transverse jet. *J. Fluid. Mech.* 575:267–305
McCann G, Bowersox R. 1996. Experimental investigation of supersonic gaseous injection into a supersonic freestream. *AIAA J.* 34:317–23
McClinton CR. 2006. *X-43–Scramjet power breaks the hypersonic barrier: Dryden Lectureship in Research for 2006*. Presented at AIAA Aerosp. Sci. Meet. Exhib., 44th, Reno, NV, AIAA Pap. 2006-1
McDaniel JC, Graves J. 1988. Laser-induced fluorescence visualization of transverse gaseous injection in a nonreacting supersonic combustor. *J. Propuls. Power* 4:591–97
McMillin BK, Seitzman JM, Hanson RK. 1994. Comparison of NO and OH planar fluorescence temperature measurements in scramjet model flowfields. *AIAA J.* 32:1945–52
Megerian S, Davitian J, de B. Alves LS, Karagozian AR. 2007. Transverse jet shear-layer instabilities. Part 1. Experimental studies. *J. Fluid. Mech.* 593:93–129
Morkovin MV, Pierce CA Jr, Craven CE. 1952. Interaction of a side jet with a supersonic main stream. *Bull. 35*, Eng. Res. Inst., Univ. Michigan
Moussa ZM, Trischka JW, Eskinazi S. 1977. The near-field in the mixing of a round jet with a cross-stream. *J. Fluid Mech.* 80:49–80
Muppidi S, Mahesh K. 2005. Study of trajectories of jets in crossflow using direct numerical simulations. *J. Fluid Mech.* 530:81–100
Muppidi S, Mahesh K. 2006. A model for the formation of the counter-rotating vortex pair in jets in crossflow. *Phys. Fluids* 18:085103
Muppidi S, Mahesh K. 2007. Direct numerical simulation of round turbulent jets in crossflow. *J. Fluid Mech.* 574:59–84

Muppidi S, Mahesh K. 2008. Direct numerical simulation of passive scalar transport in transverse jets. *J. Fluid Mech.* 598:335–60

New TH, Lim TT, Luo SC. 2003. Elliptic jets in cross-flow. *J. Fluid Mech.* 494:119–40

Orth RC, Funk JA. 1967. An experimental and comparative study of jet penetration in supersonic flow. *J. Spacecr.* 4:1236–42

Orth RC, Schetz JA, Billig FS. 1969. The interaction and penetration of gaseous jets in supersonic flow. *NASA CR-1386*, NASA, Washington, DC

Papamoschou D, Hubbard DG. 1993. Visual observations of supersonic transverse jets. *Exp. Fluids* 14:468–76

Patrick MA. 1967. Experimental investigation of the mixing and penetration of a round turbulent jet injected perpendicularly into a transverse stream. *J. Hydronaut. Div. ASCE* 45:16–31

Peterson SD, Plesniak MW. 2004. Evolution of jets emanating from short holes into crossflow. *J. Fluid Mech.* 503:57–91

Peterson DM, Subbareddy PK, Candler GV. 2006. *Assessment of synthetic inflow generation for simulating injection into a supersonic crossflow*. Presented at AIAA/AHI Space Planes Hypersonic Syst. Technol. Conf., Canberra, Austr., AIAA Pap. 2006-8128

Pope SB. 2000. *Turbulent Flows*. Cambridge, UK: Cambridge Univ. Press

Pratte BD, Baines WD. 1967. Profiles of the round turbulent jet in a cross flow. *J. Hydraul. Div. ASCE* 92:53–64

Ramsey JW, Goldstein RJ. 1970. Interaction of a heated jet with a deflecting stream. *NASA Rep. HTL-TR 92*, NASA Lewis Res. Cent., Cleveland, OH

Ricou FP, Spalding DB. 1961. Measurements of entrainment by axisymmetrical turbulent jets. *J. Fluid Mech.* 11:21–32

Rogers RC. 1971. A study of the mixing of hydrogen injected normal to a supersonic airstream. *NASA Rep. TN-D6114*, NASA Langley Res. Cent., Hampton, VA

Rothstein AD, Wantuck PJ. 1992. *A study of the normal injection of hydrogen into a heated supersonic flow using planar laser-induced fluorescence*. Presented at SAE, ASME, ASEE Joint Propuls. Conf. Exhib., 28th, Nashville, TN, AIAA Pap. 1992-3423

Santiago JG, Dutton JC. 1997. Velocity measurements of a jet injected into a supersonic crossflow. *J. Propuls. Power* 13:264–73

Sau R, Mahesh K. 2008. Dynamics and mixing of vortex rings in crossflow. *J. Fluid Mech.* 604:389–409

Sau R, Mahesh K. 2010. Optimization of pulsed jets in crossflow. *J. Fluid Mech.* 653:365–90

Schetz JA, Billig ES. 1966. Penetration of gaseous jet injected into a supersonic stream. *J. Spacecr.* 3:1658–65

Schetz JA, Billig FS. 1987. *Studies of scramjet flowfields*. Presented at SAE, ASME, ASEE Joint Propuls. Conf., 23rd, San Diego, AIAA Pap. 1987-2161

Schetz JA, Hawkins PF, Lehman H. 1967. Structure of highly underexpanded transverse jets in a supersonic stream. *AIAA J.* 5:882–84

Schetz JA, Weinraub RA, Mahaffey RE. 1968. Supersonic transverse injection into a supersonic stream. *AIAA J.* 6:933–34

Schlegel F, Wee D, Marzouk YM, Ghoniem AF. 2011. Contributions of the wall boundary layer to the formation of the counter-rotating vortex pair in transverse jets. *J. Fluid Mech.* 676:461–90

Shan JW, Dimotakis PE. 2006. Reynolds-number effects and anisotropy in transverse-jet mixing. *J. Fluid Mech.* 566:47–96

Sherif SA, Pletcher RH. 1989. Measurements of the flow and turbulence characteristics of round jets in cross-flow. *Trans. ASME J. Fluids Eng.* 111:165–71

Smith SH, Mungal MG. 1998. Mixing, structure and scaling of the jet in cross-flow. *J. Fluid Mech.* 357:83–122

Su LK, Mungal MG. 2004. Simultaneous measurement of scalar and velocity field evolution in turbulent crossflowing jets. *J. Fluid Mech.* 513:1–45

Sutton OG. 1932 A theory of eddy diffusion in the atmosphere. *Proc. R. Soc. A* 135:143–65

Sykes RI, Lewellen WS, Parker SF. 1986. On the vorticity dynamics of a turbulent jet in a cross-flow. *J. Fluid Mech.* 168:393–413

VanLerberghe WM, Santiago JG, Dutton JC, Lucht RP. 2000. Mixing of a sonic transverse jet injected into a supersonic flow. *AIAA J.* 38:470–79

Vranos A, Nolan JJ. 1965. *Supersonic mixing of a light gas and air*. Presented at AIAA Joint Propuls. Spec. Conf., Colorado Springs, CO

Yuan LL, Street RL, Ferziger JL. 1999. Large-eddy simulations of a round jet in cross-flow. *J. Fluid Mech.* 379:71–104

Zukoski EE, Spaid FW. 1964. Secondary injection of gases into a supersonic crossflow. *AIAA J.* 2:1689–996